

# (2+1)D SU(2) Yang-Mills Lattice Gauge Theory at finite density via tensor networks

Giovanni Cataldi<sup>1,2,3</sup> Giuseppe Magnifico<sup>1,2,3,4</sup> Pietro Silvi<sup>1,2,3</sup> and Simone Montangero<sup>1,2,3</sup>

<sup>1</sup>*Dipartimento di Fisica e Astronomia “G. Galilei”, Università di Padova, I-35131 Padova, Italy.*

<sup>2</sup>*Padua Quantum Technologies Research Center, Università degli Studi di Padova.*

<sup>3</sup>*Istituto Nazionale di Fisica Nucleare (INFN), Sezione di Padova, I-35131 Padova, Italy.*

<sup>4</sup>*Dipartimento di Fisica, Università di Bari, I-70126 Bari, Italy.*

(Dated: July 19, 2023)

We demonstrate the feasibility of Tensor Network simulations of non-Abelian lattice gauge theories in two spatial dimensions, by focusing on a (minimally truncated) SU(2) Yang-Mills model in Hamiltonian formulation, including dynamical matter. Thanks to our sign-problem-free approach, we characterize the phase diagram of the model at zero and finite baryon number, as a function of the bare mass and color charge of the quarks. Already at intermediate system sizes, we distinctly detect a liquid phase of quark-pair bound-state quasi-particles (baryons), whose mass is finite towards the continuum limit. Interesting phenomena arise at the transition boundary where color-electric and color-magnetic terms are maximally frustrated: for low quark masses, we see traces of potential deconfinement, while for high quark masses, we observe signatures of a possible topological order.

Non-Abelian gauge field theories, such as Quantum Chromodynamics (QCD), lay at the core of the Standard Model of particle physics. They have been extensively successful in predicting the physical phenomena of quarks and gluons with large momentum transfers, where perturbative methods apply. Conversely, at the energy scales of the hadronic world, where perturbative methods fail, robust numerical frameworks were developed, such as lattice gauge theories (LGTs) [1, 2]. Monte Carlo (MC) simulations of LGTs characterized essential phenomena such as the hadronic spectrum, the mechanism for confinement [3–5], the chiral symmetry breaking mechanism [6–9], and the role of topology in QCD at finite temperatures [10–13]. Despite an impressive number of successful predictions, MC methods are hindered by the infamous sign problem, which hampers the simulation of a wide class of physical settings described by complex or negative actions (finite charge-density phases, fermions, real-time dynamics), whose numerical investigations remain – to date – an open challenge [14, 15].

In the last decade, following Feynman’s seminal proposal and the recent fast development of quantum computers and simulators, quantum-inspired strategies attacked this challenge. On one hand side, atomic quantum simulators attempted to reproduce the quantum dynamics of lattice gauge theories [16–20]. On the other hand, Tensor Networks (TN) methods were identified as a powerful sign-problem-free numerical tool for complex lattice models [21–24]. Exploiting TN algorithms, noteworthy results have been produced for Abelian gauge theories in (1+1)D [25–39] and higher spatial dimensions [40–42]. As for non-Abelian gauge symmetries, TN-based simulations were so far limited to one spatial dimension [43–45]. In this work, we overcome such limitation: here we present the TN simulation of a (2+1)D Hamiltonian analogous to a SU(2) Yang-Mills LGT, with flavorless fermionic matter. The 2-colored quarks are discretized as staggered fermions on the sites of a square lattice, whereas the non-Abelian gauge fields live on the lattice bonds, undergoing a Kogut-Susskind dynamics similar to

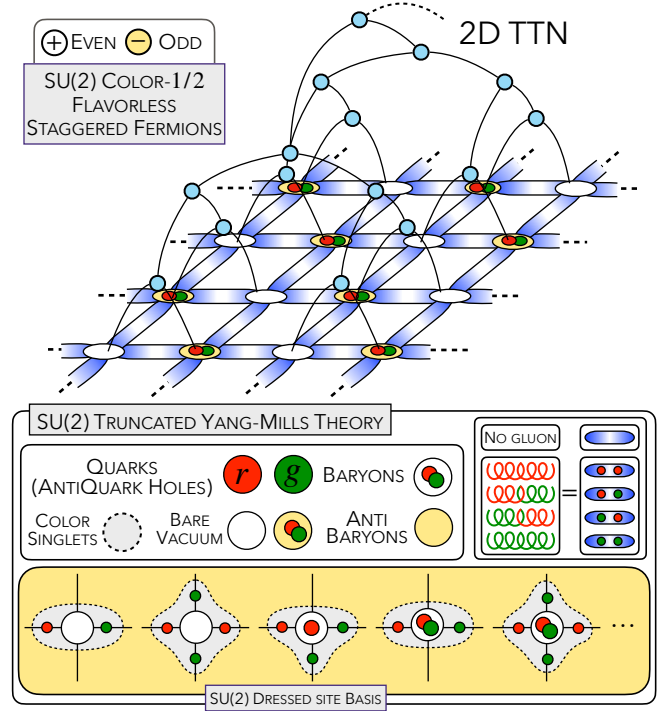


Figure 1. Sketches of TTN approach to (2+1)D SU(2) Yang-Mills LGT. Lattice sites host flavorless SU(2)-color-1/2 fermionic fields (red and green) in a staggered configuration (white and yellow). Lattice (blue) links describe gauge degrees of freedom belonging to a 5-dimensional truncated Hilbert space. SU(2) Gauss Law is implemented at each lattice site.

a quantum link formalism (QLM) [46–50]. Precisely, this study considers an electrically-truncated  $(0)-(0) \oplus (\frac{1}{2})-(\frac{1}{2})$  representation of the SU(2) gauge field, *i.e.* the smallest nontrivial representation (see Fig. 1), where gluons are hardcore bosons with a spin- $\frac{1}{2}$  color input and a spin- $\frac{1}{2}$  color output.

We report numerical simulation results for the afore-

mentioned model, using both exact diagonalization (ED) methods for small system sizes (up to  $3 \times 2$ ) and Tree Tensor Network (TTN) methods for intermediate system sizes ( $\geq 10$  matter sites). We describe several regimes of the model at equilibrium, including finite baryon number density. The analysis of the ground state properties of the system, for lattice sizes up to  $4 \times 8$  as performed here, due to the rich structure of the quantum degrees of freedom, would require  $>160$  qubits to describe on a quantum computer. We characterize the model phase diagram by evaluating multiple observables, such as energy gaps, matter/antimatter and color-charge densities, and gauge field distributions.

TNs are based on controlled wave-function variational ansatzes exploiting the area-law entanglement bounds satisfied by locally interacting many-body quantum systems. Thus, they allow an efficient representation of the low-energy sectors contributing to the equilibrium properties and (low-entangled) time evolution [51]. TN methods do not suffer from the aforementioned sign problem [52]. In this framework, ansatzes like Matrix Product States (MPS), Projected Entangled Pair States (PEPS), and Tree Tensor Networks (TTN) have found increasing applications for studying quantum many-body systems and LGTs [21, 22, 26, 27, 50, 52–55]. One main challenge for numerical and quantum simulations of gauge theories is the finite-dimensional encoding of the continuous gauge fields. A few recipes are known to achieve this reduction, from finite groups [32, 36, 56] to fusion algebra deformation [57]. We adopt an energy-cutoff truncation strategy analogous to the Quantum Link Model (QLM) [46–49], an approach already considered for practical quantum simulation of LGTs [58–66]. In this sense, the TN approach and the presented results could be used for benchmarking and validating current and future experimental implementations on quantum hardware [57, 67–77] and to systematically identify the quantum advantage threshold [78, 79].

The manuscript is organized as follows: Sec. I introduces the SU(2) Yang-Mills lattice Hamiltonian, and illustrates the rishon-based QLM [69, 80–82] we adopt, built on top of an energy-truncated Kogut-Susskind formulation [83]. In Sec. II, we present ground-state numerical simulation results for the effective Hamiltonian. In Sec. III, our conclusions and outlook are presented. Finally, the appendices contain additional technical details of the theoretical mapping and the numerical simulation settings.

## I. MODEL: LATTICE SU(2) YANG-MILLS

We numerically simulate, via Tensor Network methods, a Hamiltonian lattice-gauge model corresponding to the SU(2) Yang-Mills lattice gauge field theory at low energies. We consider flavorless fermionic matter, on a finite  $L_x \times L_y$  lattice  $\Lambda$ , and control the following parameters of the model: the quark bare mass  $m_0$ , the quark color charge  $q_c$ , the lattice spacing  $a$ , and the baryon number

density  $b$ . Sites and links are respectively identified by the couple  $(\mathbf{j}, \boldsymbol{\mu})$ , where  $\mathbf{j} = (j_x, j_y)$  is any 2D site, while  $\boldsymbol{\mu}$  is one of the two positive lattice unit vectors:  $\boldsymbol{\mu}_x = (1, 0)$ ,  $\boldsymbol{\mu}_y = (0, 1)$ . Lattice sites are occupied by matter fields, which we represent with SU(2)-color staggered (Dirac) fermions  $\psi_{\mathbf{j},\alpha}$  [84], satisfying

$$\{\hat{\psi}_{\mathbf{j},\alpha}^\dagger, \hat{\psi}_{\mathbf{j}',\beta}\} = \delta_{\mathbf{j},\mathbf{j}'} \delta_{\alpha,\beta}, \quad \text{where} \quad \alpha, \beta \in \{r, g\} \quad (1)$$

are SU(2)-colors. Then, the Hamiltonian reads:

$$\begin{aligned} \hat{H} = & + \frac{c\hbar}{2a} \sum_{\alpha,\beta} \sum_{\mathbf{j} \in \Lambda} \left[ -i \hat{\psi}_{\mathbf{j},\alpha}^\dagger \hat{U}_{\mathbf{j},\mathbf{j}+\boldsymbol{\mu}_x}^{\alpha\beta} \hat{\psi}_{\mathbf{j}+\boldsymbol{\mu}_x,\beta} \right. \\ & \left. - (-1)^{j_x+j_y} \hat{\psi}_{\mathbf{j},\alpha}^\dagger \hat{U}_{\mathbf{j},\mathbf{j}+\boldsymbol{\mu}_y}^{\alpha\beta} \hat{\psi}_{\mathbf{j}+\boldsymbol{\mu}_y,\beta} + \text{H.c.} \right] \\ & + m_0 c^2 \sum_{\mathbf{j} \in \Lambda} (-1)^{j_x+j_y} \sum_{\alpha} \hat{\psi}_{\mathbf{j},\alpha}^\dagger \hat{\psi}_{\mathbf{j},\alpha} + \hat{H}_{\text{pure}} \end{aligned} \quad (2)$$

where  $c$  is the speed of light,  $\hbar$  is the Planck constant, and  $a$  is the lattice spacing. The first two terms describe fermion-hopping between nearest-neighboring sites along the  $(\mathbf{j}, \mathbf{j} + \boldsymbol{\mu})$  lattice link. To enforce gauge symmetry, the hopping mechanism has to be mediated by the SU(2)-parallel transporter operator  $\hat{U}_{\mathbf{j},\mathbf{j}+\boldsymbol{\mu}}^{\alpha\beta}$ , acting on the gauge fields which live on the lattice links. The latter term, or staggered mass, ensures that the fermion fields, at low energies and free theory, correctly describe a Dirac 4-spinor field with bare mass  $m_0$  [2, 84, 85].

We employ the Kogut-Susskind formulation of gauge field dynamics [83] for the pure Hamiltonian  $\hat{H}_{\text{pure}}$ , due to its simplicity. Namely, we have

$$\begin{aligned} \hat{H}_{\text{pure}} = & + g^2 \frac{c\hbar}{2a} \sum_{\mathbf{j} \in \Lambda} \left( \hat{E}_{\mathbf{j},\mathbf{j}+\boldsymbol{\mu}_x}^2 + \hat{E}_{\mathbf{j},\mathbf{j}+\boldsymbol{\mu}_y}^2 \right) \\ & - g^{-2} \frac{8c\hbar}{a} \sum_{\square \in \Lambda} \sum_{\substack{\alpha,\beta, \\ \gamma,\delta}} \text{Re} \left( \begin{array}{ccc} \lrcorner & \hat{U}_{\gamma\delta}^\dagger & \lrcorner \\ \hat{U}_{\delta\alpha}^\dagger & & \hat{U}_{\beta\gamma} \\ \lrcorner & \hat{U}_{\alpha\beta} & \lrcorner \end{array} \right), \end{aligned} \quad (3)$$

where the coupling  $g(q_c, a)$  is dimensionless, but scales nonetheless with the lattice spacing  $a$  to ensure that the color charge  $q_c$  of a quark stays finite in the continuum limit. Namely, in  $D$  spatial dimensions, it should scale as  $g(q_c, a) \propto q_c a^{\frac{3-D}{2}}$  (see Appendix A).

As it is,  $\hat{H}_{\text{pure}}$  in Eq. (3) is already a frustrated quantum model even without fermion fields ( $m \rightarrow \infty$ ). The first term represents the SU(2)-electric energy density and corresponds to the quadratic Casimir operator on every link:

$$\hat{E}_{\mathbf{j},\mathbf{j}+\boldsymbol{\mu}}^2 = \left| \hat{\mathbf{L}}_{\mathbf{j},\mathbf{j}+\boldsymbol{\mu}} \right|^2 = \left| \hat{\mathbf{R}}_{\mathbf{j},\mathbf{j}+\boldsymbol{\mu}} \right|^2, \quad (4)$$

where  $\hat{\mathbf{L}}_{\mathbf{j},\mathbf{j}+\boldsymbol{\mu}}$  (resp.  $\hat{\mathbf{R}}_{\mathbf{j},\mathbf{j}+\boldsymbol{\mu}}$ ) are the group generators of the left (right) gauge transformations on the link, hermi-

tian and satisfying

$$\begin{aligned} [\hat{L}^\nu, \hat{R}^{\nu'}] &= 0 \\ [\hat{L}_{\mathbf{j},\mathbf{j}+\boldsymbol{\mu}}^\nu, \hat{L}_{\mathbf{j}',\mathbf{j}'+\boldsymbol{\mu}'}^{\nu'}] &= i\delta_{\mathbf{j}\mathbf{j}'}\delta_{\boldsymbol{\mu}\boldsymbol{\mu}'}\epsilon_{\nu\nu'}L_{\mathbf{j},\mathbf{j}+\boldsymbol{\mu}}^{\nu''} \end{aligned} \quad (5)$$

(same with  $\hat{\mathbf{R}}$ ) with  $\epsilon$  the Levi-Civita symbol. The second contribution to Eq. (3) approximates the SU(2)-magnetic energy density through the smallest Wilson loops, i.e. square gauge-invariant plaquettes made out of parallel transporters  $\hat{U}$ .

According to Wilson's formulation of LGTs, faithful representations of the local gauge field algebra satisfy

$$\begin{aligned} [\hat{L}_{\mathbf{j},\mathbf{j}+\boldsymbol{\mu}}^\nu, \hat{U}_{\mathbf{j}',\mathbf{j}'+\boldsymbol{\mu}'}^{\alpha\beta}] &= -\delta_{\mathbf{j}\mathbf{j}'}\delta_{\boldsymbol{\mu}\boldsymbol{\mu}'} \sum_\gamma \frac{\sigma_{\alpha\gamma}^\nu}{2} \hat{U}_{\mathbf{j},\mathbf{j}+\boldsymbol{\mu}}^{\gamma\beta}, \\ [\hat{R}_{\mathbf{j},\mathbf{j}+\boldsymbol{\mu}}^\nu, \hat{U}_{\mathbf{j}',\mathbf{j}'+\boldsymbol{\mu}'}^{\alpha\beta}] &= +\delta_{\mathbf{j}\mathbf{j}'}\delta_{\boldsymbol{\mu}\boldsymbol{\mu}'} \sum_\gamma \hat{U}_{\mathbf{j},\mathbf{j}+\boldsymbol{\mu}}^{\alpha\gamma} \frac{\sigma_{\gamma\beta}^\nu}{2} \end{aligned} \quad (6)$$

for  $\sigma^\nu$  Pauli matrices and a unitary and infinite dimensional parallel transporter  $\hat{U}$ :

$$\sum_{\alpha,\beta} \hat{U}_{\mathbf{j},\mathbf{j}+\boldsymbol{\mu}}^{\alpha\beta\dagger} \hat{U}_{\mathbf{j},\mathbf{j}+\boldsymbol{\mu}}^{\alpha\beta} = \mathbb{1} \quad (7)$$

To perform numerical simulations of the Hamiltonians in Eq. (2)-(3), we need to achieve a consistent yet finite truncation of the local gauge Hilbert space. We rely on the Quantum Link Model (QLM) [48] approach, which promotes the gauge field operators  $E^2$  and  $U$  to quantum spin-like operators in a finite SU(2) representation.

In this work, we consider  $(0 \otimes 0) \oplus (\frac{1}{2} \otimes \frac{1}{2})$  as the gauge field space (dimension 5), where ( $s$ ) is the irreducible spin- $s$  representation of SU(2) [46, 47]. This is the smallest representation ensuring a nontrivial contribution of all the terms in the Hamiltonian Eq. (2)-(3). The truncation keeps the electric field operator  $\hat{E}$  hermitian and protects the algebra rules of Eq. (6), but  $\hat{U}$  is no longer unitary (it loses norm on the largest spin shell). Moreover, it introduces a local energy cutoff in units of  $g^2 a^{-1}$ .

To accurately represent the full theory, for weak- $g$ , larger gauge representations are required: this increases the computational challenges but it is still potentially accessible via TNs. Finally, we define an equivalent Hamiltonian (see Appendix B) acting on logical sites built merging gauge and matter degrees of freedom in a compact dressed-site formalism [69, 80, 81], where the original non-Abelian gauge invariance is exactly rewritten into an Abelian, nearest-neighbor, diagonal selection rule, and the explicit dependence on the fermionic matter has been eliminated [40, 82, 86]. We also stress that large- $g$  regime can be addressed by exploiting perturbation theory in  $1/g^2$  (carried out in Appendix D). In this scenario, the full theory can be mapped to a good approximation into a spin-like Hamiltonian similar to a 2D anisotropic Heisenberg model [87, 88].

## II. RESULTS

This section collects the numerical results from the ground states of SU(2) Hamiltonian in Eq. (2)-(3), obtained both via Exact Diagonalization (ED) and Tree Tensor Network simulations (TTN). Hereafter, we work in Planck units ( $c = \hbar = 1$ ) and re-scale energies so that the hopping term has constant coupling  $\frac{1}{2}$ . Consequently, the other Hamiltonian terms acquire the re-scaled dimensionless couplings  $m = m_0 a$  (staggered mass),  $\frac{g^2}{2}$  (electric) and  $\frac{8}{g^2}$  (magnetic). Since  $g$  has to scale as  $g \propto a^{1/2}$  in two spatial dimensions, the continuum limit is located at  $g^2 = \alpha_c m \rightarrow 0$ , if we exclude quantum corrections to the scaling (anomalous dimension [89]). The fixed, dimensionless 'quark ratio'  $\alpha_c = g^2/m$  does not scale with the lattice spacing and is solely determined by the color charge and the bare mass of the quark (see Appendix A).

Together with the ground-state energy density  $\varepsilon = \langle \hat{H} \rangle / |\Lambda|$ , we evaluate the expectation values  $\langle \cdot \rangle$  of several local observables onto the computed ground states. Regarding gauge fields, we track the color-electric and -magnetic energy densities

$$\langle E^2 \rangle = \frac{1}{|\Lambda|} \sum_{\mathbf{j} \in \Lambda} \sum_{\boldsymbol{\mu}} \langle \hat{E}_{\mathbf{j},\boldsymbol{\mu}}^2 \rangle \quad (8)$$

$$\langle B^2 \rangle = -\frac{1}{|\square|} \sum_{\square \in \Lambda} \text{Re} \left\langle \begin{array}{c} \hat{U}^\dagger \\ \hat{U} \end{array} \right\rangle + c' \quad (9)$$

where  $|\Lambda|$  and  $|\square|$  correspond to the total number of sites and lattice plaquettes. The constant factor  $c' = \frac{1}{2}$  in Eq. (9) sets the minimum of the magnetic energy density to 0. When considering the matter, it is useful to separately measure the staggered fermion density for even (+) and odd (-) sites

$$N_\pm = \frac{1}{|\Lambda_\pm|} \sum_{\mathbf{j} \in \Lambda_\pm} \langle \hat{N}_{\mathbf{j}} \rangle = \frac{1}{|\Lambda_\pm|} \sum_{\mathbf{j} \in \Lambda_\pm} \sum_{\alpha=r,g} \langle \hat{\psi}_{\mathbf{j},\alpha}^\dagger \hat{\psi}_{\mathbf{j},\alpha} \rangle \quad (10)$$

where  $\Lambda_+$  (resp.  $\Lambda_-$ ) is the even (odd) sub-lattice. Tracking these two quantities separately gives us immediate access to the total *particle density* (quarks plus anti-quarks)

$$\varrho = N_+ - N_- + 2 \quad 0 \leq \varrho \leq 4 \quad (11)$$

as well as the *baryon number density*, (quarks minus anti-quarks divided by two)

$$b = \frac{1}{2}(N_+ + N_- - 2) \quad 0 \leq b \leq 1 \quad (12)$$

which is a good quantum number, as it is a conserved quantity tied to the global staggered fermion number conservation. We stress that, unlike quantum chromodynamics, SU(2) Yang-Mills baryons – colorless bound states of matter particles – are made by two, not three, quarks. Similarly, anti-baryons are made by two anti-

quarks. Correspondingly, mesons are made by one quark and one anti-quark as normal.

Both mesons and standalone quarks can be detected by looking at the average *color density*, that is, the quadratic Casimir operator  $|\mathbf{S}|^2$  of the matter field gauge group transformations, generated by

$$\hat{\mathbf{S}}_j = \frac{1}{2} \sum_{\alpha\beta} \hat{\psi}_{j,\alpha}^\dagger \hat{\psi}_{j,\beta} \boldsymbol{\sigma}_{\alpha\beta}, \quad \text{where } \alpha, \beta \in \{r, g\}. \quad (13)$$

Our quantitative analysis also includes the von Neumann entanglement entropy [51]

$$\mathcal{S}_A = -\text{Tr } \rho_A \log_2 \rho_A, \quad (14)$$

where  $\rho_A$  is the reduced density matrix of the partition  $A$ , which we choose exactly to be the bottom (or top) half of the system.

### A. Magneto-electric transition in the pure theory

We first focus on the pure theory ( $m = \infty$ ) under Open Boundary Conditions (OBC). According to the results shown in Fig. 2, the pure Hamiltonian displays two phases driven by  $g$ . In the small- $g$  (magnetic) phase, the plaquette interactions provide the larger contribution to the energy in Eq. (3). As such, magnetic fields are depleted, and electric fields display large quantum fluctuations (see Appendix E) and compensate for any electric activity. Conversely, in the large- $g$  (electric) phase, electric fields are energetically expensive and thus depleted in the ground state, while magnetic fields show large fluctuations.

Unlike the electric phase, which displays marginal entanglement as the ground state is almost a product state, the magnetic phase reveals an entanglement that scales with the length of the bi-partition: this behavior, signaling a sharp area-law of entanglement, suggests that the magnetic phase is likely approximated by a resonant-valence bond state of plaquettes, akin to the local structure of the ground state of the Toric Code [90].

The entanglement entropy approximates a monotonic function along  $g$ , without any peak in the transition between the two phases. This observation suggests that, for large bare masses  $m$ , this quantum phase transition is either *first order* or a *crossover*. Conversely, as shown in Appendix E), the small- $m$  scenario of the full theory peaks close to the transition, and the peak is wider and larger for smaller masses.

### B. Baryonic spectrum

For finite  $m$ , fermionic matter is included in the full Hamiltonian of Eq. (2). The baryon number density  $b$  is a quantum number associated with global symmetry, and can thus be directly encoded in the TTN ansatz. In

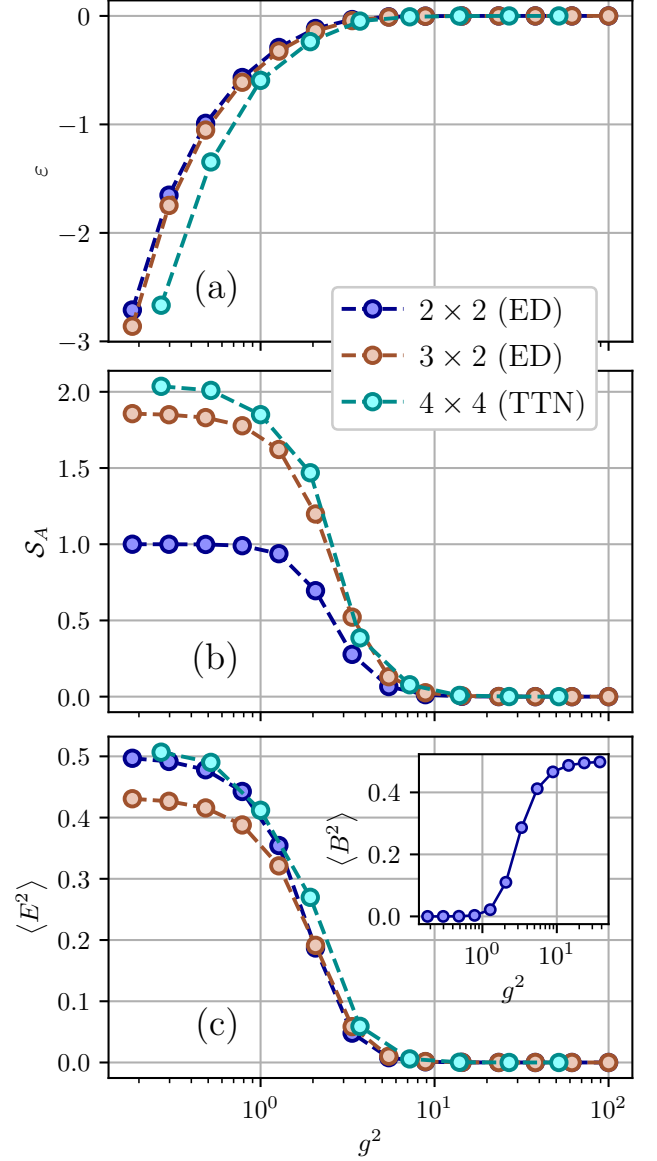


Figure 2. Numerical simulations of the pure Hamiltonian in Eq. (3) with OBC for different lattice sizes. The plots display respectively (a) the ground-state energy density  $\varepsilon$ , (b) the entanglement entropy  $\mathcal{S}_A$  of half the system, (c) the average electric energy contribution  $\langle E^2 \rangle$ , with the magnetic energy density  $\langle B^2 \rangle$  shown in the inset.

this way, we directly target the ground state within a selected baryon number density sector [24, 80].

The model is symmetric under CP, that is, mirror spatial reflection ( $j_x \rightarrow L_x - j_x$ ) times particle-hole exchange ( $\hat{\psi}_\alpha \rightarrow i\sigma_{\alpha\beta}^y \hat{\psi}_\beta^\dagger$ ) of the staggered fermions. Therefore, at negative baryon densities  $b < 0$ , the ground state is the CP-reflected of the ground state at positive baryon density  $|b|$ .

We numerically verified that the global ground state is found at null baryon density  $b = 0$  for any  $g$  and  $m$ . As



we can directly tune the baryon number of each TTN simulation, we have immediate access to the inter-sector energy gap densities by calculating the difference

$$\begin{aligned}\Delta_{|b|} &= \varepsilon_b - \varepsilon_0 = \varepsilon_{-b} - \varepsilon_0 \geq 0 \\ &= m|b| + \Delta_{|b|}^*,\end{aligned}\quad (15)$$

where we also defined the *binding energy density*  $\Delta_{|b|}^*$  by subtracting the bare mass of the corresponding excess quarks or anti-quarks.

A simple, but illustrative, analysis is to study these energy density gaps between the sector with one-baryon ( $b = 2/|\Lambda|$ ) and the vacuum sector ( $b = 0$ ), and then approach the continuum limit  $a \rightarrow 0$  at fixed ratio  $\alpha_c = g^2/m \propto q_c^2/m_0$ .

As shown in Fig. 3(a), the gap  $\Delta_{2/|\Lambda|}$  displays a clear linear scaling with  $m = m_0 a$ . In conclusion, we obtain:

$$\Delta_{2/|\Lambda|} = \kappa(\alpha_c) m_0 a \quad \text{where} \quad m_b = |\Lambda| \kappa(\alpha_c) m_0 \quad (16)$$

is the actual mass of the baryon. As it is normal for all hadrons, its mass is always greater than the bare mass of its components, thus  $\kappa \geq 1/2$ . We show this observation in Fig. 3(b), where we display  $\kappa$  as a function of  $\alpha_c$ . More interestingly, in the case of the binding energy density  $\Delta_{2/|\Lambda|}^*$  (inset of Fig. 3(b)), we observe a power-law scaling of  $\kappa^*$  in  $\alpha_c$ :

$$\kappa^* = \frac{\Delta_{2/|\Lambda|}^*}{m} = \kappa - \frac{1}{2} \quad \text{with} \quad \kappa^*(\alpha_c) \sim 0.13 \cdot \alpha_c^{0.96} \quad (17)$$

compatible with linear scaling. Such relations confirm that baryons are actual quasi-particles of the continuum theory and provide a connection to the bare quark properties ( $\alpha_c, m_0$ ). We carried out this analysis for a finite-size sample, but the baryon-to-quark mass ratio  $\kappa$  is expected to stay finite even at the thermodynamical limit.

### C. Baryon-liquid phase

Beyond energy gaps, other phase properties can be inferred when probing the observables in Eq. (8)-(14). The magneto-electric transition, driven by  $g^2$ , remains unaltered for finite  $m$  and even at finite baryon densities  $b$ , as shown in Fig. 4.

By contrast, the particle density  $\varrho$  reveals an exciting behavior as the re-scaled quark mass  $m$  is lowered. As long as  $m$  is the largest energy scale of the model ( $m \gg 1, g^2, g^{-2}$ ) the emergent behavior is relatively trivial, as a system of gapped hardcore bosons. More precisely, if  $b \geq 0$  (resp.  $b \leq 0$ ) the antimatter (matter) sites are fully emptied, while the matter (antimatter) sites host exactly  $b$  quark-pair hardcore bosons, mass gapped and with almost flat-band dynamics. The particle density  $\varrho$  confirms this interpretation, as it stays at its minimum possible value of  $\varrho \simeq \varrho_{\min}(b) = 2|b|$  and having no

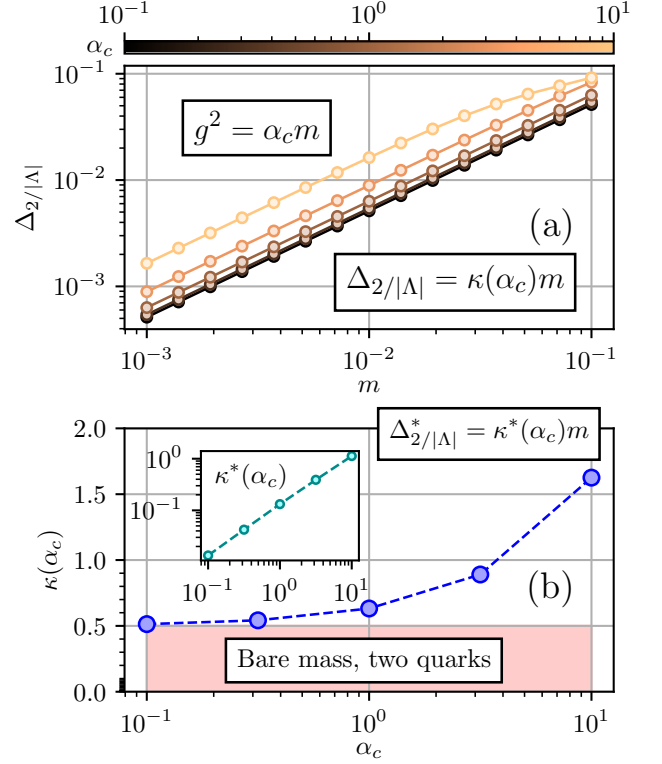


Figure 3. (a) Scaling of the inter-sector gap  $\Delta_{2/|\Lambda|}$  in Eq. (15) as a function of  $m$ , for different choices of the  $g$ -coupling  $g^2 = \alpha_c m$ . By fitting the power-law scaling of  $\Delta_{2/|\Lambda|}$  in the small- $m$  limit, we obtain the linear dependence on  $m$  shown in Eq. (16), whose slope  $\kappa$  depends on  $\alpha_c$  as shown in (b). The inset displays the corresponding  $\kappa^*$  of the binding energy density  $\Delta_{2/|\Lambda|}^*$  in Eq. (17). Results have been obtained from simulations of a  $2 \times 2$  lattice in PBC, where  $\Delta_{2/|\Lambda|} = \Delta_{|b|=0.5}$ .

fluctuations  $\delta\rho \simeq 0$  (see for instance Appendix E).

The behavior drastically changes at low masses  $m$ , in relative proximity of the transition line  $g^2 \sim 2(1)$ , as shown in Fig. 5. In fact, for  $m$  lower than a critical value  $m^*(g)$ , we see a sharp growth of the particle density  $\rho$  and its on-site fluctuations  $\delta\rho$ , which become similar in magnitude (see Appendix E). Even though we do not have access to long-range correlation functions at these limited system sizes, this observation is a strong hint of superfluidity of the phase, where we expect the quasi-particle excitations to be gapless (in the rescaled units).

To deeper investigate the nature of these quasi-particles we track the matter-color density  $|\mathbf{S}|^2$  (see Fig. 7 and Appendix E). There is a very narrow region around the magneto-electric transition where colored matter emerges (maybe a possible deconfined critical boundary). Elsewhere, especially towards the continuum limit, the color density stays  $|\mathbf{S}|^2 = 0$ . We must conclude that the gapless quasi-particles must be made by on-site pairs of quarks or anti-quarks. As such, we can regard the low-mass phase,  $m < m^*(g)$ , as a *gapless baryon liquid*.

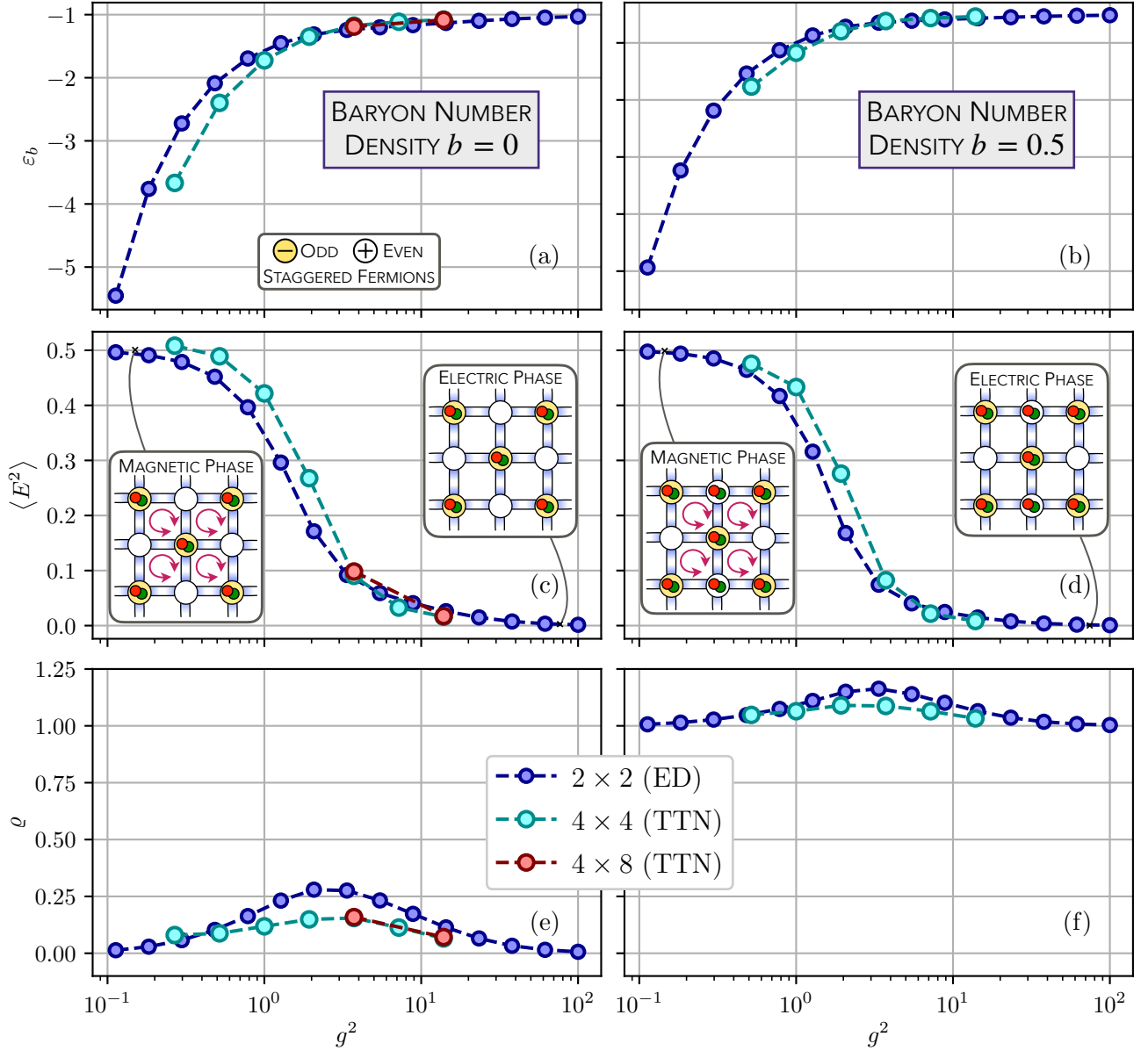


Figure 4. Numerical results of the full  $SU(2)$  Hamiltonian in Eq. (2) with OBC and baryon number density  $b = 0$  (left column) and  $b = 0.5$  (right column). The plots display respectively: (a)-(b) the ground-state energy density  $\varepsilon_b$ , (c)-(d) the average electric energy contribution  $\langle E^2 \rangle$  in Eq. (8), enlightening the transition between the magnetic (purple fluxes) and the electric (no fluxes) phases discussed in Sec. II A, and (e)-(f) the average particle density  $\varrho$  in Eq. (11), which appears peaked in the  $g$ -transition. The pictorial lattice configurations in the finite baryon density  $b = 0.5$  represent states with  $b$  extra gapped hardcore local bosons with low dynamics compatible with the two electric/magnetic phases.

Using a finite-size scaling technique (shown in Fig. 5(b)) we are able to characterize  $m^*$  as a power-law function of  $g^2$ , where a numerical regression yields

$$m^*(g^2) \simeq 0.267(4) \cdot (g^2)^{1.03(2)}, \quad (18)$$

which is less than  $2\sigma$  deviation from a linear scaling. If we now assume that the linear scaling holds, then there must be a critical quark ratio  $\alpha_c^* = 3.75(6)$  that determines the behavior when approaching the continuum limit (recall

that  $\alpha_c^*$  depends only on quark color-charge and bare mass, see Appendix A). Namely, for strong color charges  $\alpha_c > \alpha_c^*$  the baryon fluid at  $a \rightarrow 0$  is gapless, while for weak charges  $\alpha_c < \alpha_c^*$  the baryon fluid is gapped. We recall that we are working with energy scales rescaled by  $a$ , thus only quasiparticles that we identify as gapless at the continuum limit will survive as finite energy excitations in natural units.

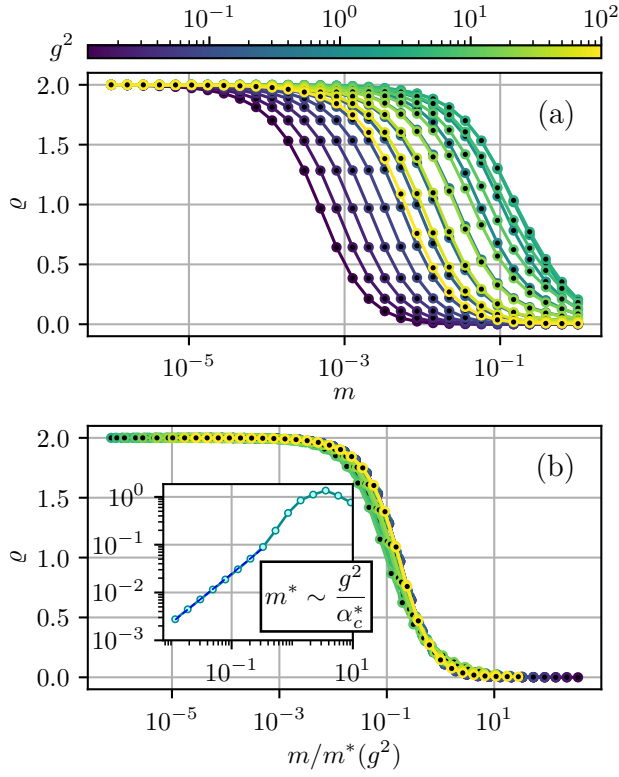


Figure 5. (a) Scaling of the particle density defined in Eq. (11) as a function of  $m$  for different values of the gauge coupling  $g$ . (b) All the  $\rho(m)$  curves of the particle density collapse on a single one simply by re-scaling the mass  $m$  by a factor  $m^*$  displaying a power-law scaling in  $g^2$  (see the inset). By fitting this scaling we extract Eq. (18), whose error bars have been computed exploiting error propagation onto the covariance matrix of the fit. Results obtained from simulations on a  $2 \times 2$  lattice in OBC at baryon density  $b = 0$ .

#### D. Non-local/Topological properties

A relevant analysis that can be carried out in Yang-Mills theories is the characterization of topological properties at the critical point, and the investigation of whether some form of topological order emerges within or without deconfined phases [91, 92]. While the simplified model we considered does not support the existence of a deconfined phase in proximity to the continuum limit, it is still possible to characterize some topological properties by evaluating non-local order parameters. As detailed in Appendix C, the pure theory Eq. (3), corresponding to  $m \rightarrow \infty$ , protects a topological symmetry, which exists only under periodic boundary conditions. Such symmetry identified by the topological invariants (string operators)  $\mathbb{P}_{x,y}$  defined in Eq. (C5)-(C4) and forming a  $\mathbb{Z}_2 \times \mathbb{Z}_2$  group.

By selecting each quantum number(s) for this symmetry group, we can evaluate inter-sector and intra-sector energy gaps, and verify the presence of quasi-degeneracies,

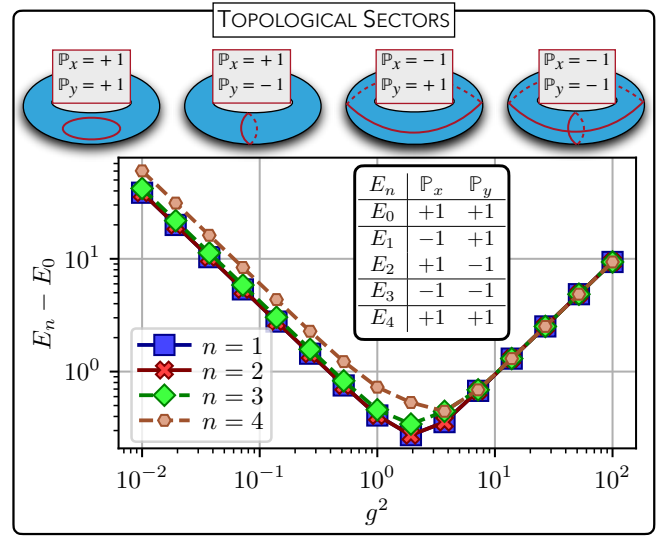


Figure 6. Energy gaps between the first excited levels and the ground state of Eq. (3) in PBC, for a  $2 \times 2$  lattice. Every state belongs to one of the topological sectors sketched on top: closed red curves on the blue torus correspond to  $SU(2)$  electric-loop excitations.

signatures of a potential spontaneous breaking of the topological symmetry group, and thus of topological order. As shown in Fig. 6, when approaching the transition point from the large- $g$  phase, both inter-sector and intra-sector gaps reach a minimum, signaling a possible degeneracy lifted by finite-size effects. However, both gaps re-open while moving towards the small- $g$  phase. This observation suggests that topological order does not survive for  $g^2 \ll 2$ .

The addition of dynamical matter removes the topological invariants  $\mathbb{P}_{x,y}$  from being symmetries of the model, due to the hopping term inverting the string parity (see Appendix C and Fig. 11). In the large- $m$  limit, where the particle density is vanishing, the full theory approaches the pure one, and the topological invariants become good quantum numbers again.

#### E. (2+1)D $SU(2)$ Yang-Mills LGT Phase Diagram

By collecting all the previous observations, we can outline in Fig. 7 the full phase diagram of the 2D  $SU(2)$  Yang-Mills Hamiltonian in Eq. (2)-(3) around zero baryon density  $b = 0$  (where the baryon mass gap opens).

We observed that the presence of fermionic degrees of freedom affects only marginally the behavior of the gauge degrees of freedom of Eq. (8)-(9), albeit the magnetoelectric transition becomes smoother at lower  $m$  values (see also Appendix E).

For  $m$  sufficiently large,  $m > m^*(g)$  the matter fields play a minor role (trivial phase). The Hamiltonian recovers the topological properties of the pure theory Sec. IID (check also Appendix C) but no spontaneous topologi-

cal order survives outside the magneto-electric transition  $g^2 \sim 2(1)$ .

Conversely, for small masses  $m < m^*(g)$ , [93], we observe an emergent color-density of the matter fields, only in the proximity of the magneto-electric transition. Such observation is compatible with the existence of a deconfined critical phase in the region where electric and magnetic fields are maximally frustrated (see also Fig. 13). Elsewhere, the system behaves like a gapless liquid of colorless baryons and anti-baryons. The collective behavior towards the continuum limit is particularly intriguing, as it can exhibit both trivial or baryon superfluid phase depending on the quark ratio  $\alpha_c$ .

### III. CONCLUSIONS

In this work, we have demonstrated the feasibility of TN simulations of non-Abelian Yang-Mills LGTs in two spatial dimensions, including dynamical matter. We investigated in detail both the zero and finite baryon number density regimes, where Monte Carlo methods are severely limited due to the sign problem. In this regard, our results confirm TN methods as an efficient and reliable approach to addressing non-perturbative phenomena of LGTs, capable of accessing strong-coupling regimes as well as finite baryon number densities. From the numerical estimations of various observables, we have sketched the zero-temperature phase diagram of a (2+1)D hardcore-gluon SU(2) Yang-Mills Hamiltonian, while inferring quite a few qualitative and quantitative observations concerning these phases.

First of all, when approaching the continuum limit ( $a \rightarrow 0$  at fixed  $m_0, \alpha_c$ ) SU(2) baryons and anti-baryons become the actual quasiparticles of the theory. Interestingly, baryons seem to be able to condense into a superfluid phase for a sufficiently large quark ratio  $\alpha_c \geq \alpha_c^*(m_0)$ , that is, if their color charge is strong enough.

In the parameter regime at  $g^2 \sim 2(1)$ , where the electric term and the magnetic term are maximally frustrated, and electric and magnetic field fluctuations are commensurate, we witnessed more exotic physics: at low quark masses, the system manifests colorful matter sites, possibly indicating a quark-deconfined regime, such as a quark-gluon plasma. At high quark masses, the system encounters a degeneracy between topological sectors (string symmetries in periodic boundary conditions), possibly signaling the emergence of a topological order reminiscent of the Toric code.

From a theoretical perspective, the studied Hamiltonian describes the interaction between flavorless 2-color fermionic matter and hardcore boson gauge fields (encoded as  $(0)-(0) \oplus (\frac{1}{2})-(\frac{1}{2})$  representation). Considering larger representations of the gauge field Hilbert space (following the same prescription derived in Appendix B) would be a natural extension of the present work and an improved approximation of the continuous gauge field theory. Similarly, the numerical simulations we carried

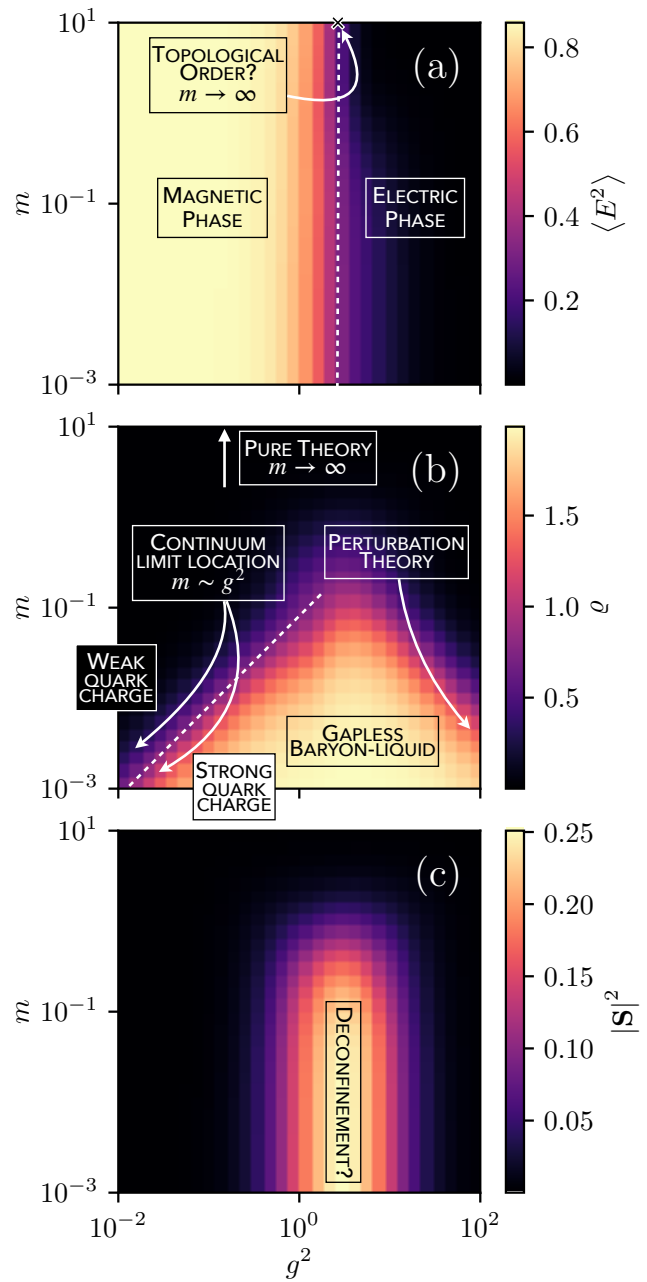


Figure 7. Phase diagram  $(g^2, m)$  of the full SU(2) Hamiltonian in Eq. (2)-(3) in the sector with zero baryon number density from (a) the average electric energy density in Eq. (8), (b) the average particle density in Eq. (11), and (c) the matter color density defined in Eq. (13). Phases are marked according to the discussion in Sec. II, and Appendix E.

out with TTN were limited to finite system sizes, up to 32 lattice sites hosting the matter fields and 64 lattice bonds hosting the gauge fields. Of course, gaining access to even larger system sizes would be a substantial advantage, as it would enable the characterization of correlation functions not distorted by finite-size effects. To overcome these limitations (finite gauge representation, finite system sizes) further developments of the numer-



ical simulation architecture are required: On the hardware side, the possibility of running the computation on a (pre)exascale HPC environment, while on the software side the development of new and improved TN-based algorithms. The latter will be achieved, for instance, with the use of the augmented TTN ansatz, which drastically enhances the capability of representing area law-states in high dimensions [94]. These steps will be fundamental for the long-term goal of applying TN methods to large-scale lattice QCD in three spatial dimensions and ultimately address open, secular research problems, such as confinement and asymptotic freedom.

From an experimental viewpoint, the dressed-site formalism developed to build the Hamiltonian could be in principle encoded on quantum hardware. In this perspective, the results and the methods presented in this work represent essential tools for benchmarking and validating current and future experimental implementations [75, 95].

#### IV. ACKNOWLEDGEMENTS

We are thankful to Luca Tagliacozzo, Torsten V. Zache, Marcello Dalmonte, and Elisa Ercolessi for their enlightening suggestions concerning the topological characterization of the model. G.C. thanks Marco Rigobello for all the precious discussions and the use of the SIMSIO GitHub repository for managing the I/O of numerical simulations [96]. The authors are also grateful to the Mainz Institute for Theoretical Physics (MITP) of the DFG Cluster of Excellence PRISMA\* (Project ID 39083149), for its hospitality and its partial support during the completion of this work. This work is partially supported by the Italian PRIN2017, Fondazione CARIPARO, the INFN project QUANTUM, the QuantERA projects QuantHEP and T-NISQ; the Quantum Flagship - PASQuanS2; the European Union - NextGenerationEU project CN00000013 - Italian Research Center on HPC, Big Data and Quantum Computing. We acknowledge computational resources by the Cloud Veneto, CINECA, the BwUniCluster, the University of Padova Strategic Research Infrastructure Grant 2017: CAPRI: Calcolo ad Alte Prestazioni per la Ricerca e l'Innovazione, and the WCRI-Quantum Computing and Simulation Center of Padova University.

##### Appendix A: Dimensional analysis and continuum limit

The simplest way to carry out dimensional analysis, while locating the continuum limit in the space of coupling parameters, is to consider the electric energy

$$H_{\text{elec}} = \frac{\epsilon_c}{2} \int \mathcal{E}^2(\mathbf{x}) (d\mathbf{x})^D \quad (\text{A1})$$

for a system of  $D$  spatial dimensions. We can express, in SI units, the color-vacuum permittiv-

ity  $\epsilon_c$ , which has a physical dimension of  $[\epsilon_c] = (\text{charge})^2 (\text{length})^{2-D} (\text{energy})^{-1}$ , as well as the color-electric field  $\mathcal{E}$ , which has physical dimension of  $[\mathcal{E}] = (\text{charge})^{-1} (\text{length})^{-1} (\text{energy})$ . To recast the problem onto a spatial lattice we can easily substitute

$$\int (d\mathbf{x})^D \rightarrow a^D \sum_{\mathbf{j}, \mu} \quad \text{and} \quad \mathcal{E}^2(\mathbf{x}) \rightarrow \frac{q_c^2 a^{2-2D}}{\epsilon_c^2} E_{\mathbf{j}, \mu}^2 \quad (\text{A2})$$

where we introduced a lattice spacing  $a$ , a quark color-charge  $q_c$ , in such a way to obtain a dimensionless  $E_{\mathbf{j}, \mu}^2$  as in Eq. (4). It is then possible to recast the charge in dimensionless units, precisely as

$$g = q_c \frac{a^{\frac{3-D}{2}}}{\sqrt{\hbar c \epsilon_c}}, \quad (\text{A3})$$

yielding the conversion

$$H_{\text{elec}} = \frac{q_c^2 a^{2-D}}{2\epsilon_c} \sum_{\mathbf{j}, \mu} E_{\mathbf{j}, \mu}^2 = g^2 \frac{c\hbar}{2a} \sum_{\mathbf{j}, \mu} E_{\mathbf{j}, \mu}^2 \quad (\text{A4})$$

compatible with Eq. (3). Now, if we do not consider quantum corrections to the scaling (see by contrast Refs. [10, 25]), it makes sense to assume that in the continuum  $a \rightarrow 0$  limit the color-charge  $q_c$  stays finite. In two spatial dimensions  $D = 2$ , this requirement implies that  $g^2$  has to scale linearly with  $a$ . One can write  $g = \sqrt{a/a_0}$  where  $a_0 = \hbar c \epsilon_c / q_c^2$  is the (inverse square) color-charge written as a length scale.

In this framework, while moving toward the continuum limit  $a \rightarrow 0$ , the electric energy coupling  $g^2 c\hbar / 2a = c\hbar / 2a_0$  and the staggered mass coupling  $m_0 c^2$  stay at the fixed ratio of

$$\alpha_c = \frac{q_c^2}{2m_0 c^2 \epsilon_c} \quad (\text{A5})$$

which is determined by the quark bare mass  $m_0$  and its color charge  $q_c$ . It is a dimensionless parameter not scaling with the lattice spacing, thus it plays a role equivalent to the fine-structure constant (but for SU(2)-YM interaction and in  $D = 2$ ).

##### Appendix B: Fermionic compact representation of the local SU(2) gauge-invariant site

As aforementioned in Sec. I, to make LGT Hamiltonians suitable for TN methods as well as for quantum hardware, we need to deal with a finite-dimensional Hilbert space. In this section, we outline and detail our description of non-Abelian LGTs in high-dimensional lattices based on a rishon formulation of the Quantum Link Model (QLM) [48]. In a nutshell, by merging matter and (truncated) gauge degrees of freedom, we obtain a fermionic compact representation of the local SU(2) gauge-invariant site and then an operative Hamiltonian

that is used for the simulations discussed in Sec. II.

### 1. SU(2) Quantum Link Model inspired

The starting point of our construction is inspired by the QLM formalism, according to which, the gauge fields  $E^2$  and  $U$  in Eq. (2)-(3) are promoted to quantum spin-like operators in a finite SU(2) representation. As stated in Sec. I, we focus on the smallest non-trivial representation of the gauge fields, i.e. a 5-dimensional gauge-link Hilbert space obtained from the  $(0)-(0) \oplus (\frac{1}{2})-(\frac{1}{2})$  irreducible representation of SU(2) [46, 47]. Then, the states describing the gauge-link activity can be referred to as the following spin states:

$$\mathcal{H}_{\text{link}} = \{|00\rangle, |rr\rangle, |rg\rangle, |gr\rangle, |gg\rangle\}, \quad (\text{B1})$$

where  $g$  and  $r$  are SU(2) colors. Within this representation, we can then define the corresponding versions of the truncated gauge fields. First, we expect the parallel transport  $U_{\mathbf{j}, \mathbf{j}+\boldsymbol{\mu}}^{\alpha\beta}$  to be (i) *mutually bosonic*, as it commutes with all the fermionic matter-fields operators

$$[U_{\mathbf{j}, \mathbf{j}+\boldsymbol{\mu}}^{\alpha\beta}, \psi_{\mathbf{j}, \alpha}^{(\dagger)}] = 0 \quad \forall \mathbf{j}, \forall \boldsymbol{\mu}, \forall \alpha, \beta \quad (\text{B2})$$

and (ii) *purely local*, as its link-algebra commutes with the one of any other link:

$$[U_{\mathbf{j}, \mathbf{j}+\boldsymbol{\mu}}^{\alpha\beta}, U_{\mathbf{j}', \mathbf{j}'+\boldsymbol{\mu}'}^{\gamma\delta}] = 0 \quad \forall \mathbf{j} \neq \mathbf{j}', \boldsymbol{\mu} \neq \boldsymbol{\mu}', \forall \alpha, \beta, \gamma, \delta \quad (\text{B3})$$

Moreover,  $\forall \mathbf{j}, \forall \boldsymbol{\mu} \in \Lambda$ , we expect

$$\sum_{\alpha, \beta=r, g} \psi_{\mathbf{j}, \alpha}^{\dagger} U_{\mathbf{j}, \mathbf{j}+\boldsymbol{\mu}}^{\alpha\beta} \psi_{\mathbf{j}+\boldsymbol{\mu}, \beta} \quad (\text{B4})$$

to be invariant under SU(2) transformations of  $\alpha$  and  $\beta$  separately. This implies for  $U_{\mathbf{j}, \mathbf{j}+\boldsymbol{\mu}}^{\alpha\beta}$  to satisfy the gauge transformations presented in Eq. (6). In our specific truncated gauge-basis, the generators of the left- and right-handed groups of SU(2) transformations,  $\hat{\mathbf{L}}$  and  $\hat{\mathbf{R}}$ , read:

$$\mathbf{L} = \frac{1}{2} \left( \begin{array}{c|c} 0 & 0 \\ \hline 0 & \vec{\sigma} \otimes \mathbb{1} \end{array} \right) \quad \mathbf{R} = \frac{1}{2} \left( \begin{array}{c|c} 0 & 0 \\ \hline 0 & \mathbb{1} \otimes \vec{\sigma} \end{array} \right) \quad (\text{B5})$$

satisfying the same algebra of Eq. (5). Under these constraints, the parallel transporter for a  $(0)-(0) \oplus (\frac{1}{2})-(\frac{1}{2})$  irreducible SU(2) representation reads [97]:

$$U_{\alpha\beta} = \frac{1}{2} \left( \begin{array}{c|cccc} 0 & +\delta_{\alpha r} \delta_{\beta g} & -\delta_{\alpha r} \delta_{\beta r} & +\delta_{\alpha g} \delta_{\beta g} & -\delta_{\alpha g} \delta_{\beta r} \\ \hline -\delta_{\alpha g} \delta_{\beta r} & 0 & 0 & 0 & 0 \\ -\delta_{\alpha g} \delta_{\beta g} & 0 & 0 & 0 & 0 \\ +\delta_{\alpha r} \delta_{\beta r} & 0 & 0 & 0 & 0 \\ +\delta_{\alpha r} \delta_{\beta g} & 0 & 0 & 0 & 0 \end{array} \right) \quad (\text{B6})$$

where the 1/2 prefactor ensures that the hopping term preserves the state norm on its support. Correspondingly, the quadratic Casimir operator in Eq. (4):

$$E^2 = \frac{3}{4} \left( \begin{array}{c|ccccc} 0 & 0 & 0 & 0 & 0 \\ \hline 0 & 1 & 0 & 0 & 0 \\ 0 & 0 & 1 & 0 & 0 \\ 0 & 0 & 0 & 1 & 0 \\ 0 & 0 & 0 & 0 & 1 \end{array} \right) \quad (\text{B7})$$

At this point, the SU(2) quantum-many-body (QMB) state of the system describing matter sites and gauge-link degrees of freedom can be expressed as

$$|\Psi\rangle = \bigotimes_{\mathbf{j} \in \Lambda} \bigotimes_{k=x,y} |\text{site}\rangle_{\mathbf{j}} \otimes |\text{link}\rangle_{\mathbf{j}, \mathbf{j}+\boldsymbol{\mu}_k} \quad (\text{B8})$$

where we restrict the Hilbert space associated with matter sites only to SU(2)-color 1/2 flavorless particles:

$$\mathcal{H}_{\text{site}} = \{|\Omega\rangle, \psi_{\mathbf{r}}^{\dagger} |\Omega\rangle, \psi_{\mathbf{g}}^{\dagger} |\Omega\rangle, \psi_{\mathbf{r}}^{\dagger} \psi_{\mathbf{g}}^{\dagger} |\Omega\rangle\} \quad (\text{B9})$$

Among all the possible QMB states in Eq. (B8), we need to select only the ones, where the SU(2)-Gauss law is satisfied on every lattice site (see the (e) panel of Fig. 8). On the trails of [69, 80], we develop a model that is genuinely equivalent to the Hamiltonians in Eq. (2)-(3), but with a Hilbert space that is made out of only gauge invariant states (SU(2) singlets). Such an approach prevents us from imposing SU(2) Gauss Law by applying several long-range Hamiltonian penalties which significantly impact numerical efficiency. In a nutshell, we *dress* every physical matter site with the information related to its adjacent gauge links. A pictorial scheme of our recipe is sketched in Fig. 8: (a) starting from the original description (matter site & gauge links), (b) we populate each half-link with a fermionic rishon mode  $\zeta$  and (c) constrain the link dynamics accordingly to the original SU(2) theory. At this point, (d) we merge the half-links to the attached matter site, ending up in *dressed sites* that automatically satisfy SU(2) Gauss law.

### 2. SU(2) fermionic rishon modes

Let us then start writing the parallel transport as

$$\hat{U}_{\mathbf{j}, \mathbf{j}+\boldsymbol{\mu}}^{\alpha\beta} = \hat{\zeta}_{\mathbf{j}, \boldsymbol{\mu}}^{\alpha} \left( \hat{\zeta}_{\mathbf{j}+\boldsymbol{\mu}, -\boldsymbol{\mu}}^{\beta} \right)^{\dagger} \quad (\text{B10})$$

where  $\hat{\zeta}_{\mathbf{j}, \boldsymbol{\mu}}^{\alpha}$  and  $\hat{\zeta}_{\mathbf{j}+\boldsymbol{\mu}, -\boldsymbol{\mu}}^{\beta}$  are two fermionic rishon modes living on the two halves of the link  $(\mathbf{j}, \mathbf{j}+\boldsymbol{\mu})$ . Formally, requiring the  $\zeta$ -rishons to be fermionic implies that they satisfy Fermi statistics among them and with matter fields. Namely,  $\forall \mathbf{j}, \forall \boldsymbol{\mu}, \in \Lambda$ , we require

$$\{\hat{\zeta}_{\mathbf{j}, \boldsymbol{\mu}}^{\alpha}, \hat{\zeta}_{\mathbf{j}+\boldsymbol{\mu}, -\boldsymbol{\mu}}^{\beta}\} = 0 \quad \{\hat{\zeta}_{\mathbf{j}, \boldsymbol{\mu}}^{\alpha}, \hat{\psi}_{\mathbf{j}, \beta}\} = 0 \quad (\text{B11})$$

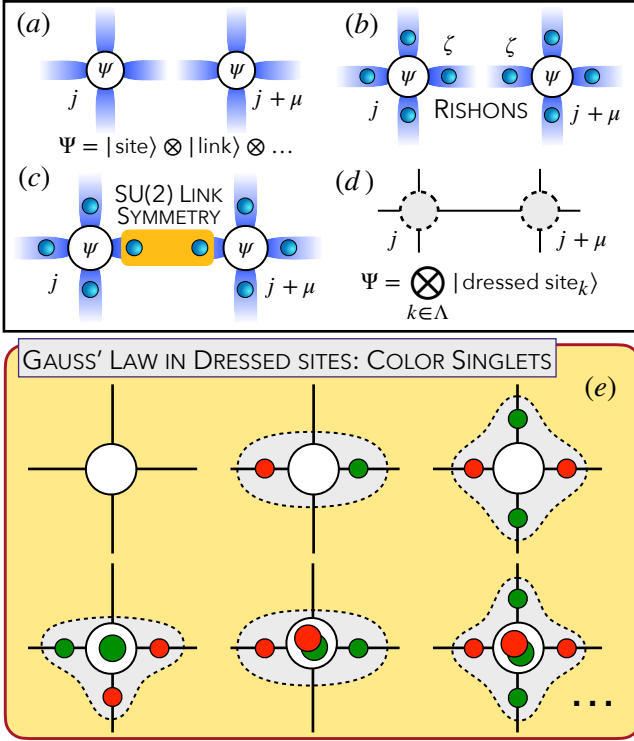


Figure 8. Sketched representation of the approach developed in Appendix B: (a) starting from the original formulation with matter sites and gauge links, (b) populate them with rishon modes  $\zeta$  defined in Eq. (B15), (c) constrain their dynamics with the SU(2) link symmetry in Eq. (B25), and (d) merge them with matter fields into dressed SU(2) gauge-singlets.

In order Eq. (B11) to be satisfied, we need to arbitrarily sort all the fermions (rishon modes on the links and matter fields on the sites) along a certain path in the lattice  $\Lambda$ . Then, when considering the tensor product of consecutive fermionic operators, we apply the proper anti-commutation rules. Namely, the action of a generic fermionic operator  $\hat{F}_j$  on the  $j^{\text{th}}$  position along the path reads:

$$\hat{F}_j = \dots P_{j-2} \otimes P_{j-1} \otimes F_j \otimes \mathbb{1}_{j+1} \otimes \mathbb{1}_{j+2} \dots \quad (\text{B12})$$

where  $P_j = P_j^\dagger = P_j^{-1}$  is a fermion parity operator that gets inverted after the action of a fermionic operator:

$$\{P_j, F_j\} = 0 \quad [P_j, F_{j' \neq j}] = 0 \quad \forall j, j' \in \Lambda \quad (\text{B13})$$

Being fermions, Eq. (B12) holds for  $\psi$ -matter fields and  $\zeta$ -rishon modes as well. As for Dirac fermions, we have:

$$\hat{\psi}_{\text{Dirac}} = \begin{pmatrix} 0 & 1 \\ 0 & 0 \end{pmatrix}_F \quad P_\psi = \begin{pmatrix} +1 & 0 \\ 0 & -1 \end{pmatrix} \quad (\text{B14})$$

where the subscript  $F$  is a reminder that the  $\hat{\psi}$  matrix is meant 'as a fermion', with the global action in Eq. (B12). As for  $\zeta$ -rishons, we define the parity operator with an

even (+1) parity sector on *integer* spin representations and odd (−1) sector on *semi-integer* spin ones. In the case of the smallest truncation  $s = (0) \oplus (\frac{1}{2})$ , we have:

$$\hat{\zeta}_r = \frac{1}{\sqrt{2}} \begin{pmatrix} 0 & 1 & 0 \\ 0 & 0 & 0 \\ 1 & 0 & 0 \end{pmatrix}_F \quad \hat{\zeta}_g = \frac{1}{\sqrt{2}} \begin{pmatrix} 0 & 1 & 0 \\ -1 & 0 & 0 \\ 0 & 0 & 0 \end{pmatrix}_F \quad (\text{B15})$$

with the corresponding parity operator:

$$P_\zeta = \begin{pmatrix} 1 & 0 & 0 \\ 0 & -1 & 0 \\ 0 & 0 & -1 \end{pmatrix} \quad (\text{B16})$$

Then, the parallel transporter  $\hat{U}_{j,j+\mu}^{\alpha\beta}$  in Eq. (B10) reads:

$$\begin{aligned} \hat{U}_{j,j+\mu}^{\alpha\beta} &= \hat{\zeta}_{j,\mu}^\alpha \left( \hat{\zeta}_{j+\mu,-\mu}^\beta \right)^\dagger \\ &= (\zeta_{j,\mu}^\alpha \otimes \mathbb{1}_{j+\mu,-\mu}) \cdot (P_{\zeta,j,\mu} \otimes \zeta_{j+\mu,-\mu}^{\beta\dagger}) \\ &= \zeta_{j,\mu}^\alpha \cdot P_{\zeta,j,\mu} \otimes \mathbb{1}_{j+\mu,-\mu} \cdot \zeta_{j+\mu,-\mu}^{\beta\dagger} \end{aligned} \quad (\text{B17})$$

satisfying the same properties in Eq. (B2) and Eq. (B3).

### 3. SU(2) rishon algebra

The generator of the SU(2) gauge rotations upon the  $\zeta$ -rishon space can be written as the block-diagonal direct sum of spin matrices  $\mathbf{S}_j$  in consecutive  $j$ -representations from the smallest ( $j = 0$ ) to the largest one ( $j = k$ ):

$$\hat{\mathbf{T}}_k = \bigoplus_{j=0}^k \mathbf{S}_j = \text{diag}(\mathbf{S}_0, \mathbf{S}_{1/2}, \dots, \mathbf{S}_k) \quad (\text{B18})$$

In the smallest truncation of SU(2), with  $s = (0) \oplus (\frac{1}{2})$ , the generator reads:

$$T_{1/2}^x = \begin{pmatrix} 0 & 1 \\ 0 & 1 \\ 1 & 0 \end{pmatrix} \quad T_{1/2}^y = \begin{pmatrix} 0 & 1 \\ 0 & -i \\ i & 0 \end{pmatrix} \quad T_{1/2}^z = \begin{pmatrix} 0 & 1 \\ 1 & 0 \\ 0 & -1 \end{pmatrix}$$

One can then check that  $\zeta$ -rishons in Eq. (B15) transform in a covariant way under  $\hat{\mathbf{T}}_{1/2}$ . In particular,  $\forall \alpha \in \{r, g\}$ :

$$[\hat{T}^z, \hat{\zeta}_\alpha] = -\frac{1}{2} \sum_\beta \sigma_{\alpha\beta}^z \hat{\zeta}_\beta \quad [\hat{T}^x, \hat{\zeta}_\alpha] = -\frac{1}{2} \sum_\beta \sigma_{\alpha\beta}^x \hat{\zeta}_\beta \quad (\text{B19})$$

Closing the algebra, one gets:

$$[\hat{\mathbf{T}}, \hat{\zeta}_a] = -\frac{1}{2} \sum_b \vec{\sigma}_{ab} \hat{\zeta}_b \quad (\text{B20})$$

$$[\hat{\mathbf{T}}, \hat{\zeta}_\alpha^\dagger] = -\left([\hat{\mathbf{T}}, \hat{\zeta}_\alpha]\right)^\dagger = \frac{1}{2} \sum_\beta \hat{\zeta}_\beta^\dagger \sigma_{\beta\alpha} \quad (\text{B21})$$

Moreover,  $\hat{\mathbf{T}}$  is genuinely *local*, as for  $\forall \mathbf{j} \neq \mathbf{j}' \forall \mu \neq \mu'$ :

$$[\hat{\mathbf{T}}_{\mathbf{j}+\mu}, \hat{\zeta}_{\mathbf{j}+\mu'}^\alpha] = [\hat{\mathbf{T}}_{\mathbf{j}+\mu}, \hat{\psi}_{\mathbf{j}'}] = 0 \quad (\text{B22})$$

We can easily recover the left- and right-handed sides generators of the gauge field at link  $(\mathbf{j}, \mathbf{j} + \mu)$  as:

$$\hat{\mathbf{L}}_{\mathbf{j}, \mu} = \hat{\mathbf{T}}_{\mathbf{j}, +\mu} \otimes \mathbb{1}_{\mathbf{j}+\mu, -\mu} \quad \hat{\mathbf{R}}_{\mathbf{j}, \mu} = \mathbb{1}_{\mathbf{j}, +\mu} \otimes \hat{\mathbf{T}}_{\mathbf{j}+\mu, -\mu} \quad (\text{B23})$$

In these terms, the parallel transport defined in Eq. (B10) has the same SU(2) algebra of  $U^{\alpha\beta}$  defined in Eq. (B6).

#### 4. SU(2) link symmetry

By definition, the spin-Hilbert space of every side of the link  $(\mathbf{j}, \mathbf{j} + \mu)$  hosting a rishon mode is 3-dimensional:

$$\mathcal{H}_{\mathbf{j}, \mu} = \{|0\rangle, |r\rangle, |g\rangle\} = \mathcal{H}_{\mathbf{j}+\mu, -\mu} \quad (\text{B24})$$

Correspondingly, the Hilbert space of the whole link  $\mathcal{H}_{\text{link}} = \mathcal{H}_{\mathbf{j}, \mu} \otimes \mathcal{H}_{\mathbf{j}+\mu, -\mu}$  has 9 states. To recover the original 5-dimensional space in Eq. (B1), we use another feature of the SU(2) group. Namely, as it admits a *quasi-real* representation (i.e. the fundamental and the anti-fundamental representations of SU(2) coincide), we have to select only the link configurations where the two rishons are in the same SU(2) representation [97].

Such a constraint can be obtained by requiring that the quadratic Casimir operator of the two sides of the link coincide. Namely, we have to impose that:

$$|\mathbf{L}_{\mathbf{j}, +\mu}|^2 - |\mathbf{R}_{\mathbf{j}+\mu, -\mu}|^2 = 0 \quad (\text{B25})$$

where  $\mathbf{L}$  and  $\mathbf{R}$  are the ones defined in Eq. (B23). As long as this link constraint is satisfied, the parallel transport  $\hat{U}_{\alpha\beta} = \hat{\zeta}_\alpha \hat{\zeta}_\beta^\dagger$  is proven to perfectly coincide with the one in Eq. (B6). Correspondingly, the quadratic Casimir operator of the whole  $(\mathbf{j}, \mathbf{j} + \mu)$  link in Eq. (4) can be expressed as:

$$\begin{aligned} \hat{E}_{\mathbf{j}, \mathbf{j}+\mu}^2 &= \frac{1}{2} \left[ |\hat{\mathbf{L}}_{\mathbf{j}, +\mu}|^2 + |\hat{\mathbf{R}}_{\mathbf{j}+\mu, -\mu}|^2 \right] \\ &= \frac{1}{2} \left[ |\hat{\mathbf{T}}_{\mathbf{j}, +\mu}|^2 \otimes \mathbb{1}_{\mathbf{j}+\mu, -\mu} + \mathbb{1}_{\mathbf{j}, +\mu} \otimes |\hat{\mathbf{T}}_{\mathbf{j}+\mu, -\mu}|^2 \right] \end{aligned} \quad (\text{B26})$$

which looks explicitly symmetric under link reversal.

#### 5. Towards an operative Hamiltonian

We are then ready to rewrite the SU(2) lattice Yang-Mills Hamiltonian in Eq. (2) in terms of the fermionic rishon

modes  $\zeta$ . Namely:

$$\begin{aligned} \hat{H} &= \frac{1}{2} \sum_{\alpha, \beta} \sum_{\mathbf{j} \in \Lambda} \left[ -i \hat{\psi}_{\mathbf{j}, \alpha}^\dagger \hat{\zeta}_{\mathbf{j}, \mu_x}^\alpha \hat{\zeta}_{\mathbf{j}+\mu_x, -\mu_x}^{\beta\dagger} \hat{\psi}_{\mathbf{j}+\mu_x, \beta} \right. \\ &\quad \left. - (-1)^{j_x+j_y} \hat{\psi}_{\mathbf{j}, \alpha}^\dagger \hat{\zeta}_{\mathbf{j}, \mu_y}^\alpha \hat{\zeta}_{\mathbf{j}+\mu_y, -\mu_y}^{\beta\dagger} \hat{\psi}_{\mathbf{j}+\mu_y, \beta} + \text{H.c.} \right] \\ &\quad + m \sum_{\mathbf{j} \in \Lambda} (-1)^{j_x+j_y} \sum_{\alpha} \hat{\psi}_{\mathbf{j}, \alpha}^\dagger \hat{\psi}_{\mathbf{j}, \alpha} + \hat{H}_{\text{pure}} \end{aligned} \quad (\text{B27})$$

where the pure Hamiltonian reads:

$$\begin{aligned} \hat{H}_{\text{pure}} &= + \frac{3g^2}{16} \sum_{\alpha} \sum_{\mathbf{j}, \mu} \hat{E}_{\mathbf{j}, \mathbf{j}+\mu}^2 \\ &\quad + \frac{8}{g^2} \sum_{\square \in \Lambda} \sum_{\substack{\alpha, \beta, \\ \gamma, \delta}} \text{Re} \left( \begin{array}{cc} \ulcorner & (\hat{\zeta}_\gamma \hat{\zeta}_\delta^\dagger)^\dagger \quad \urcorner \\ (\hat{\zeta}_\delta \hat{\zeta}_\alpha^\dagger)^\dagger & \hat{\zeta}_\beta \hat{\zeta}_\gamma^\dagger \\ \llcorner & \hat{\zeta}_\alpha \hat{\zeta}_\beta^\dagger \quad \lrcorner \end{array} \right) \end{aligned} \quad (\text{B28})$$

We then merge the rishon mode of every half-link with its closest neighboring matter site, ending up in dressed sites like in Fig. 8. A general dressed-site state reads:

$$\left| \hat{\zeta}_{\mathbf{j}, -\mu_x} \begin{pmatrix} \hat{\zeta}_{\mathbf{j}, +\mu_y} \\ \hat{\psi}_{\mathbf{j}, r} \hat{\psi}_{\mathbf{j}, g} \end{pmatrix} \hat{\zeta}_{\mathbf{j}, +\mu_x} \right\rangle \quad \text{where} \quad \left| \begin{array}{c} 5 \\ 2 \ (0, 1) \ 4 \\ 3 \end{array} \right\rangle \quad (\text{B29})$$

is the internal order to be used as in Eq. (B12) when defining operators acting inside the dressed sites. For instance, if we introduce:

$$\begin{aligned} \hat{Q}_{\mathbf{j}, \pm\mu}^\dagger &= \sum_{\alpha} \hat{\psi}_{\mathbf{j}, \alpha}^\dagger \hat{\zeta}_{\mathbf{j}, \pm\mu}^\alpha \quad \hat{D}_{\mathbf{j}} = \sum_{\alpha} \hat{\psi}_{\mathbf{j}, \alpha}^\dagger \hat{\psi}_{\mathbf{j}, \alpha} \\ \hat{C}_{\mathbf{j}, \mu_1, \mu_2} &= \sum_{\alpha} \hat{\zeta}_{\mathbf{j}, \mu_1}^\alpha \hat{\zeta}_{\mathbf{j}, \mu_2}^\alpha \quad \hat{\Gamma}_{\mathbf{j}} = \frac{1}{2} \sum_{\alpha, \mu} |\hat{\mathbf{T}}_{\mathbf{j}, \mu}|^2 \end{aligned} \quad (\text{B30})$$

then, the Hamiltonian in Eq. (B27)-(B28) reads:

$$\begin{aligned} \hat{H} &= + \frac{1}{2} \sum_{\mathbf{j} \in \Lambda} \left[ -i \hat{Q}_{\mathbf{j}, +\mu_x}^\dagger \hat{Q}_{\mathbf{j}+\mu_x, -\mu_x} + \right. \\ &\quad \left. - (-1)^{j_x+j_y} \hat{Q}_{\mathbf{j}, +\mu_y}^\dagger \hat{Q}_{\mathbf{j}+\mu_y, -\mu_y} + \text{H.c.} \right] \\ &\quad + m \sum_{\mathbf{j} \in \Lambda} (-1)^{j_x+j_y} \hat{D}_{\mathbf{j}} + \hat{H}_{\text{pure}} \end{aligned} \quad (\text{B31})$$

$$\hat{H}_{\text{pure}} = \frac{3g^2}{16} \sum_{\mathbf{j} \in \Lambda} \hat{\Gamma}_{\mathbf{j}} - \frac{8}{g^2} \sum_{\square \in \Lambda} \text{Re} \left( \begin{array}{cc} \hat{C}_\ulcorner & \hat{C}_\urcorner \\ \hat{C}_\llcorner & \hat{C}_\lrcorner \end{array} \right) \quad (\text{B32})$$

From a numerical perspective, to satisfy the link constraint in Eq. (B25), we add to the operative Hamiltonian in Eq. (B31)-(B32) the following penalty term:

$$\begin{aligned} h_{\mathbf{j}, \mathbf{j}+\mu}^{\text{link sym}} &= \alpha \hat{W}_{\mathbf{j}, \mathbf{j}+\mu} \\ &= \alpha \left( |\hat{\mathbf{T}}_{\mathbf{j}, \mu}|^2 - |\hat{\mathbf{T}}_{\mathbf{j}+\mu, -\mu}|^2 \right)^2 \end{aligned} \quad (\text{B33})$$

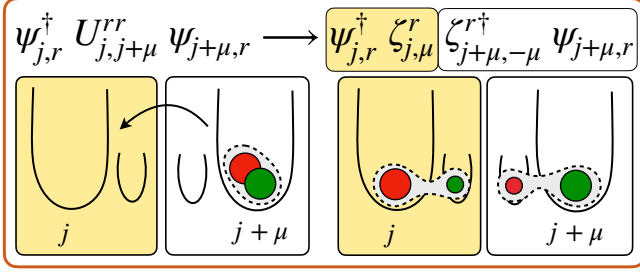


Figure 9. Representation of the matter-gauge interaction. Within the dressed site formalism, the hopping always involves an even number of fermions (the physical ones plus the link rishon modes).

As long as  $\eta$  is enough larger than the Hamiltonian couplings, Eq. (B25) is minimized and we are safely describing the original SU(2) Hamiltonian in Eq. (2)-(3). In our simulations, we choose  $\eta = 10 \cdot \max\left(\frac{3g^2}{16}, \frac{4}{g^2}, m\right)$ .

## 6. Defermionization for free

Not surprisingly, our dressed-site Hamiltonian in Eq. (B31)-(B32) is completely *bosonic*, as all the operators in (B30) are made out of pairs of fermions (matter field + rishon, pairs of matter fields, or rishon pairs). Then, the algebra of fermionic degrees of freedom is completely hidden inside each dressed site and there is no more need to face anti-commutation rules (see Fig. 9). In the  $(0)-(0) \oplus (\frac{1}{2})-(\frac{1}{2})$  truncation of SU(2), the local Hilbert space of every dressed site in Eq. (B29) of the full Hamiltonian has 30 gauge invariant states, whereas, restricting to the pure theory, the local Hilbert space is 9-dimensional.

Such an approach is inspired by [69, 80–82] and confirms to be reliable when dealing with gauge theories and dynamical matter interacting in high-dimensional lattices. Therein, due to the presence of long-range strings of operators, the use of Jordan-Wigner transformation [98] or parity operators as in Eq. (B12) is extremely inefficient from a numerical and experimental perspective. So far, only a few alternative techniques [99–101] have been developed.

## Appendix C: Non-local/topological properties

In this section, we address the topological properties of the (2+1)D SU(2) Yang-Mills LGT. In particular, we show that the pure theory in Eq. (3) displays a non-local  $\mathbb{Z}_2 \times \mathbb{Z}_2$  symmetry whose topological sectors closes as approaching the  $g$ -transition. Such a topological structure disappears in the full Hamiltonian Eq. (2) but can be recovered in the infinite mass limit. We stress that the topological symmetry is completely *independent* of

the chosen truncation of the SU(2) gauge Hilbert space developed throughout Appendix B.

Let us start searching for some topological invariants. The right candidates involve the rishon parity operators  $P_\zeta$  introduced in Eq. (B16). Thanks to the link symmetry in Eq. (B25), we can extend such a definition to the whole link  $(\mathbf{j}, \mathbf{j}+\boldsymbol{\mu})$  and consider the corresponding parity operator  $P_{\mathbf{j}, \mathbf{j}+\boldsymbol{\mu}}$ . As aforementioned, it returns (+1) for *integer* and (−1) for *semi-integer* SU(2) representations. In our 5-dimensional  $(0)-(0) \oplus (\frac{1}{2})-(\frac{1}{2})$  SU(2) truncated Hilbert space, such an operator reads:

$$P_{\mathbf{j}, \mathbf{j}+\boldsymbol{\mu}} = \begin{pmatrix} +1 & 0 & 0 & 0 & 0 \\ 0 & -1 & 0 & 0 & 0 \\ 0 & 0 & -1 & 0 & 0 \\ 0 & 0 & 0 & -1 & 0 \\ 0 & 0 & 0 & 0 & -1 \end{pmatrix} \quad \forall \mathbf{j}, \forall \boldsymbol{\mu} \quad (\text{C1})$$

By definition,  $P_{\mathbf{j}, \mathbf{j}+\boldsymbol{\mu}}$  commutes with the Casimir operator in Eq. (B7), as both are diagonal in the link basis:

$$[P_{\mathbf{j}, \mathbf{j}+\boldsymbol{\mu}}, E_{\mathbf{j}, \mathbf{j}+\boldsymbol{\mu}}^2] = 0 \quad \forall \mathbf{j}, \forall \boldsymbol{\mu} \quad (\text{C2})$$

Rather,  $P_{\mathbf{j}, \mathbf{j}+\boldsymbol{\mu}}$  anti-commutes with the parallel transport  $U$  (and  $U^\dagger$ ), as its action on the link decreases (respectively increases) the SU(2) link-representation by 1/2:

$$\{P_{\mathbf{j}, \mathbf{j}+\boldsymbol{\mu}}, U_{\mathbf{j}, \mathbf{j}+\boldsymbol{\mu}}^{(\dagger)}\} = 0 \quad \forall \mathbf{j}, \forall \boldsymbol{\mu} \in \Lambda \quad (\text{C3})$$

Then, let us consider our 2D lattice  $\Lambda$  in PBC and introduce the consecutive action of the horizontal link parity operators along a vertical loop in  $\Lambda$  (see orange links in Fig. 10). Namely, we define:

$$\begin{aligned} \mathbb{P}_y &\equiv \bigotimes_{k=0}^{|\Lambda_y|-1} P_{\mathbf{j}+k\boldsymbol{\mu}_y, \mathbf{j}+k\boldsymbol{\mu}_y+\boldsymbol{\mu}_x} \\ &= P_{\mathbf{j}, \mathbf{j}+\boldsymbol{\mu}_x} \otimes P_{\mathbf{j}+\boldsymbol{\mu}_y, \mathbf{j}+\boldsymbol{\mu}_y+\boldsymbol{\mu}_x} \otimes \dots \end{aligned} \quad (\text{C4})$$

Correspondingly, the consecutive action of the vertical link parity operator along a horizontal loop in  $\Lambda$  (see green links in Fig. 10) is

$$\begin{aligned} \mathbb{P}_x &\equiv \bigotimes_{k=0}^{|\Lambda_x|-1} P_{\mathbf{j}+k\boldsymbol{\mu}_x, \mathbf{j}+k\boldsymbol{\mu}_x+\boldsymbol{\mu}_y} \\ &= P_{\mathbf{j}, \mathbf{j}+\boldsymbol{\mu}_y} \otimes P_{\mathbf{j}+\boldsymbol{\mu}_x, \mathbf{j}+\boldsymbol{\mu}_x+\boldsymbol{\mu}_y} \otimes \dots \end{aligned} \quad (\text{C5})$$

It is clear that both the  $\mathbb{P}_x$  and  $\mathbb{P}_y$  operators remain unaffected by the action of the electric field along any one of their steps, as their parity does not get flipped. Correspondingly, any plaquette term  $B_\square^2$  of the magnetic interaction applied on the chain where  $\mathbb{P}_x$  or  $\mathbb{P}_y$  is evaluated flips the parity of two consecutive steps of the chain so that the overall sign is left unchanged. Namely:

$$[\mathbb{P}_\mathbf{j}, E_{\mathbf{j}, \mathbf{j}+\boldsymbol{\mu}}^2] = 0 = [\mathbb{P}_\mathbf{j}, B_\square^2] \quad \forall \mathbf{j}, \square \in \Lambda \quad (\text{C6})$$



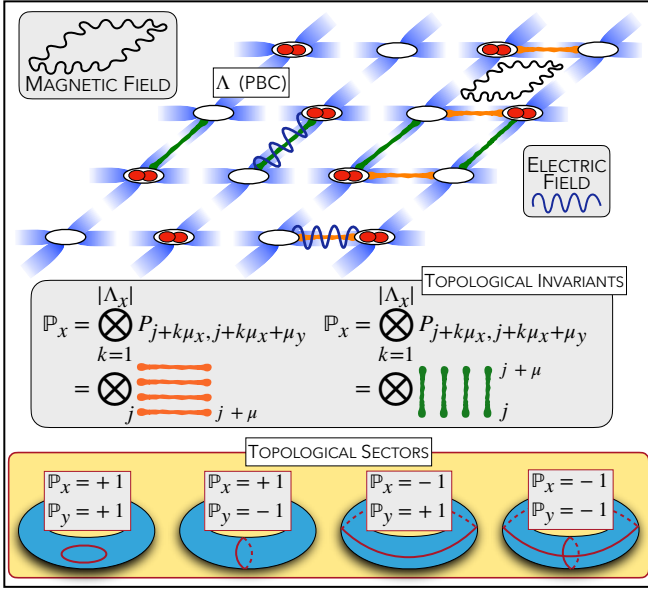


Figure 10. Pictorial representations of the topological invariants defined in Eq. (C4) and Eq. (C5) on a lattice  $\Lambda$  in PBC (i.e. a torus). The topological sectors of Eq. (C8) are sketched in the yellow panel: closed red curves on the blue torus  $\Lambda$  correspond to  $SU(2)$  loop excitations.

We conclude that  $\mathbb{P}_x$  and  $\mathbb{P}_y$  are generators of two symmetries of the pure Hamiltonian in Eq. (3):

$$[\mathbb{P}_x, H_{\text{pure}}] = 0 \quad [\mathbb{P}_y, H_{\text{pure}}] = 0 \quad (\text{C7})$$

and we can refer to them as *topological invariants*. The whole symmetry group is then  $\mathbb{Z}_2 \times \mathbb{Z}_2$ , as we have  $[\mathbb{P}_x, \mathbb{P}_y] = 0 \quad \forall x, y \in \Lambda$ . Therefore, any physical state  $|\Psi\rangle$  of the pure theory in Eq. (3) lies in one of the sectors of  $\mathbb{P}_x$  and  $\mathbb{P}_y$  sketched in the yellow panel of Fig. 10. The distinction between different symmetry sectors is in terms of the number of *non-removable loop excitations* displayed by the state. With *loop excitations*, we refer to closed magnetic strings (red circles in the blue torus of the yellow panel of Fig. 10) displayed by the state on its topological geometry. In particular, *non-removable* loops are the ones that cannot be removed through homotopies, i.e. without modifying the topology of the system.

Then, any state with an *even* a number of horizontal (vertical) non-removable loop excitations lies in the *even* sector of the vertical  $\mathbb{P}_y$  (horizontal  $\mathbb{P}_x$ ) topological invariant. Correspondingly, any state with an *odd* number of non-removable loop excitations lies in the *odd* sector of the proper topological invariant. Hence,  $\forall k \in \{x, y\}$ :

$$\langle \Psi | \mathbb{P}_k | \Psi \rangle = \lambda \quad \text{where} \quad \lambda \in \begin{array}{c|c} \mathbb{P}_x & \mathbb{P}_y \\ \hline +1 & +1 \\ +1 & -1 \\ -1 & +1 \\ -1 & -1 \end{array} \quad (\text{C8})$$

Such symmetry explicitly disappears in the full Hamiltonian Eq. (2) because of the hopping terms, as each of them includes a single parallel transport  $U$  that flips one link parity along the line where  $\mathbb{P}_x$  or  $\mathbb{P}_y$  are defined. However, in the large- $m$  limit, where the full Hamiltonian Eq. (2) falls back into the pure theory in Eq. (3), we expect to recover the same topological invariants (at least in the ground-state).

To check numerically the previous statements, we would need to measure the topological invariants on the low energy states of the Hamiltonians in Eq. (B31)-Eq. (B32). Within our dressed site formalism, Eq. (C4) and Eq. (C5) can be expressed just as chains of single-site operators along one of the two sides of the links. Indeed, as long as the  $SU(2)$  link-symmetry in Eq. (B25) is satisfied throughout via Eq. (B33), the information about every link-parity is present in both the attached neighboring sites.

As shown in Fig. 6, the topological sectors of the first 4 lowest eigenstates of the pure theory in PBC belong to a different topological sector of Eq. (C8). Moreover, the eigenstates are sorted in increasing energy according to the table in Eq. (C8). In particular,  $E_1 = E_2$  only in the case of isotropic geometries, as non-removable loop excitations along the two directions are equally expensive in energy. In the case of an-isotropic lattices, where  $|\Lambda|_x \neq |\Lambda|_y$ , non-removable loop excitations along different axes are shifted in energy.

As for the full theory, we restrict our simulations to the zero charge density sector of a  $2 \times 2$  lattice in PBC with  $m \in [10^{-2}, 10^{+2}]$ .

In Fig. 11, we look at the distance between the exact *even* topological sector of  $\mathbb{P}_y (+1)$  and the corresponding value measured on the ground state. That gap gets larger when approaching the  $g$ -transition while vanishing far from the latter. Moreover, as aforementioned, in the large-mass  $m$  limit, we recover the full symmetry sector of the pure theory.

#### Appendix D: Large- $g$ phase via perturbation theory

In the large- $g$  limit, we can address the full Hamiltonian in the zero-density sector by exploiting perturbation theory. In this regime, we can rewrite Eq. (B31) as

$$H \sim [H_0 + (H_{\text{matter}} + H_{\text{x-hop}} + H_{\text{y-hop}} + H_{\text{plaq}})] = \sum_{j \in \Lambda} [h_j^0 + h_j^{\text{matter}} + h_j^{\text{x-hop}} + h_j^{\text{y-hop}} + h_{j, \square}^{\text{plaq}}] \quad (\text{D1})$$

where  $h_0$  is the single-site unperturbed Hamiltonian:

$$h_j^0 = \frac{3g^2}{16} \Gamma_j \quad (\text{D2})$$

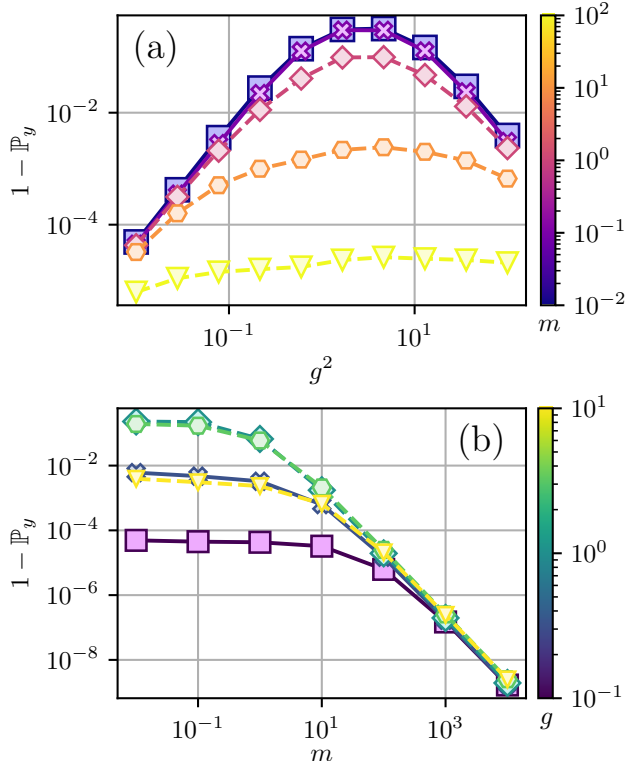


Figure 11. Distance between the ground-state  $\mathbb{P}_y$ -topological invariant in the full theory and the corresponding one of the pure theory for different  $m$ -values (a) and  $g$ -couplings (b). Results obtained from simulations in a  $2 \times 2$  lattice with PBC at  $b = 0$ .

while the perturbative terms read:

$$h_j^{\text{matter}} = m(-1)^{j_x + j_y} D_j \quad (\text{D3})$$

$$h_j^{\text{x-hop}} = \frac{1}{2} \left[ -i Q_{j,+\mu_x}^\dagger Q_{j+\mu_x,-\mu_x} + \text{H.c.} \right] \quad (\text{D4})$$

$$h_j^{\text{y-hop}} = \frac{1}{2} \left[ -(-1)^j Q_{j,+\mu_y}^\dagger Q_{j+\mu_y,-\mu_y} + \text{H.c.} \right] \quad (\text{D5})$$

$$h_{j,\square}^{\text{plaq}} = -\frac{8}{g^2} \begin{pmatrix} C_\top & C_\gamma \\ C_\perp & C_\beta \end{pmatrix} \quad (\text{D6})$$

In the large- $g$  limit, we expect the  $0^{\text{th}}$  order ground-state  $|E_0\rangle$  not to display gauge activity, as the electric interaction is energetically penalized. Then, the effective Hilbert space of the dressed sites reduces just to states with singlets in the matter fields. Namely, in terms of the sectors of the local charge density operator, we have only

$$|0\rangle \equiv \begin{vmatrix} 0 & & \\ 0 & 0 & 0 \\ 0 & & \end{vmatrix} \quad \text{and} \quad |2\rangle \equiv \begin{vmatrix} 0 & & \\ 0 & \textcolor{red}{r}g & 0 \\ 0 & & \end{vmatrix} \quad (\text{D7})$$

Therefore, at the  $0^{\text{th}}$ -order, the single-site ground-state  $|E_0\rangle$  can be expressed as a linear combination of Eq. (D7)

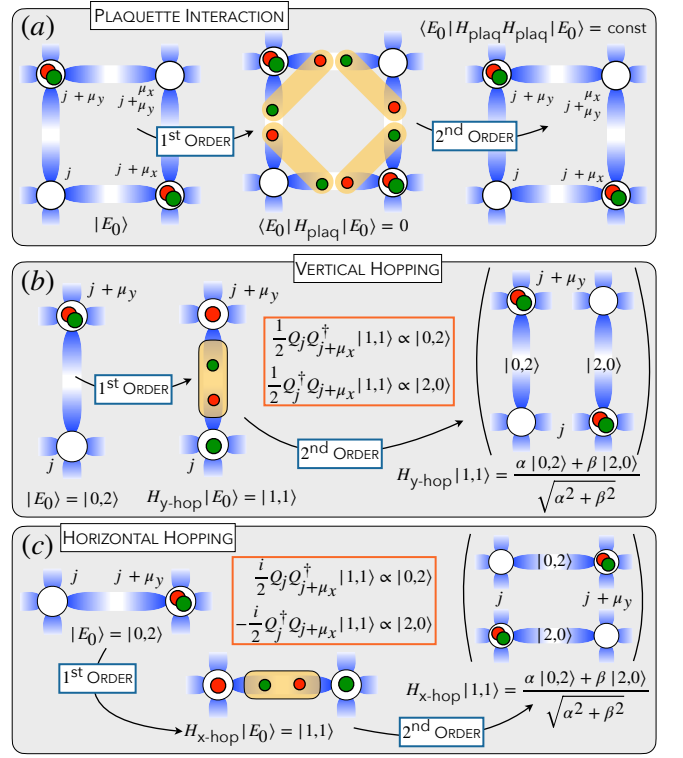


Figure 12. Graphical representation of the 1<sup>st</sup> and 2<sup>nd</sup> order perturbative effects of the magnetic and the hopping terms to the ground state of Eq. (D2).

with energy  $E_0 = 0$ :

$$|E_0\rangle = \alpha |0\rangle + \beta |2\rangle \quad \text{with} \quad \sqrt{\alpha^2 + \beta^2} = 1 \quad (\text{D8})$$

At the 1<sup>st</sup> perturbative order, we have to separately consider the action of every single term in Eq. (D3)-(D6). As for the plaquette term in Eq. (D6), we expect it to yield a vanishing contribution. Indeed, if we refer to  $|E_0\rangle$  as a single-plaquette ground state, then we have:

$$\begin{aligned} \langle E_0 | h^{\text{plaq}} | E_0 \rangle &= \langle E_0 | \left( -\frac{8}{g^2} \right) \left( \frac{1}{\sqrt{2}} \right)^4 | E_1 \rangle \\ &= -\frac{2}{g^2} \langle E_0 | E_1 \rangle = 0 \end{aligned} \quad (\text{D9})$$

since the plaquette-state  $|E_1\rangle$  is orthogonal to the ground state  $|E_0\rangle$ , as all its links are electrically active (see Fig. 12). The factor  $1/\sqrt{2}$  is due to each single corner operator  $C$  defined in Eq. (B30) and acting on the corresponding empty corner of the plaquette state  $|E_0\rangle$ .

As for the hopping terms, we focus on the effective Hilbert space of the joint neighboring sites  $\mathbf{j}$  and  $\mathbf{j} + \boldsymbol{\mu}$ :

$$\mathcal{H}_{\mathbf{j},\mathbf{j}+\boldsymbol{\mu}}^{\text{eff}} = \{|0,0\rangle, |0,2\rangle, |2,0\rangle, |2,2\rangle\} \quad \forall \mathbf{j}, \forall \boldsymbol{\mu} \quad (\text{D10})$$

where we labeled the states  $|\mathbf{j}, \mathbf{j} + \boldsymbol{\mu}\rangle$  in terms of the only two possible single-site states in Eq. (D7). First of all,

we notice that  $|0, 0\rangle$  and  $|2, 2\rangle$  are completely decoupled from the other two states, since  $\forall \mu$ :

$$Q_{j,+\mu}^\dagger Q_{j+\mu,-\mu} |0, 0\rangle = Q_{j,+\mu}^\dagger Q_{j+\mu,-\mu} |2, 2\rangle = 0 \quad (\text{D11})$$

Then, the only relevant matrix element of the effective (perturbed) hopping-Hamiltonian are the following ones:

$$\begin{aligned} Q_{j,+\mu}^\dagger Q_{j+\mu,-\mu} |0, 2\rangle &= (-1)^2 |1, 1\rangle \\ Q_{j,+\mu} Q_{j+\mu,-\mu}^\dagger |2, 0\rangle &= (-1)^2 |1, 1\rangle \end{aligned} \quad \forall j, \forall \mu \quad (\text{D12})$$

where  $|1, 1\rangle$  is figured in Fig. 12, while the  $(-1)$  factor is due to the action of a single arrival operator  $Q_{j,\mu}^{(\dagger)}$  defined in Eq. (B30) on the states in Eq. (D7). Clearly, since

$$\langle 0, 2 | 1, 1 \rangle = 0 = \langle 2, 0 | 1, 1 \rangle, \quad (\text{D13})$$

none of the hopping Hamiltonians Eq. (D4)-(D5) do provide any  $1^{st}$ -order correction to  $H_0$  in Eq. (D2).

The only relevant  $1^{st}$  order term is the one related to  $H_{\text{matter}}$ , as it acts just on the matter fields without yielding any gauge activity. Moreover, it removes the ground-state degeneracy of Eq. (D8) by favoring a staggered configuration to the lattice, namely:

$$|E_1(j)\rangle = \delta_{1,(-1)^{j_x+j_y}} |0\rangle + \delta_{-1,(-1)^{j_x+j_y}} |2\rangle \quad (\text{D14})$$

where  $\delta_{ij}$  is the Kronecker delta function. However, for sufficiently small values of the mass  $m$ , the staggering effect is irrelevant, and the degeneracy of Eq. (D8) is restored. Therefore, in the small- $m$  limit, the first relevant perturbative order is the  $2^{nd}$  one.

As for the plaquette interaction, the  $2^{nd}$  order does not remove the ground-state degeneracy, as it completely restores  $|E_0\rangle$  providing just an energy shift. Namely, the  $2^{nd}$  order perturbative corrections to the single-site ground-state energy reads:

$$\begin{aligned} E_2^{\text{plaq}} &= \frac{1}{4} \langle E_0 | h_{\text{plaq}} [E_0 - H_0]^{-1} h_{\text{plaq}} | E_0 \rangle \\ &= \frac{1}{4} \left( -\frac{2}{g^2} \right) \langle E_0 | h_{\text{plaq}} [E_0 - H_0]^{-1} | E_1 \rangle \\ &= -\frac{1}{2g^2} \langle E_0 | h_{\text{plaq}} \left[ -\frac{3g^2}{16} \sum_{j \in \square} \Gamma_j \right]^{-1} | E_1 \rangle \quad (\text{D15}) \\ &= -\frac{1}{2g^2} \left( -8 \cdot \frac{3g^2}{16} \right)^{-1} \langle E_0 | h_{\text{plaq}} | E_1 \rangle \\ &= -\frac{1}{3g^4} \left( -\frac{2}{g^2} \right) \langle E_0 | E_0 \rangle = \boxed{\frac{2}{3g^6}} \end{aligned}$$

where  $[\hat{O}]^{-1}$  is the Moore-Penrose inverse and the initial  $1/4$  factor is put to get the single-site energy out of the one of a plaquette.

As for the hopping terms, because of Eq. (D11)-(D12),

$\forall k \in \{x, y\}$ , the only relevant terms are the diagonal ones

$$\begin{aligned} &\frac{1}{2} \langle 0, 2 | h^{\text{hop}} [E_0 - H_0]^{-1} h^{\text{hop}} | 0, 2 \rangle \\ &= \frac{1}{2} \langle 2, 0 | h^{\text{hop}} [E_0 - H_0]^{-1} h^{\text{hop}} | 2, 0 \rangle \end{aligned} \quad (\text{D16})$$

and the off-diagonal ones:

$$\begin{aligned} &\frac{1}{2} \langle 0, 2 | h^{\text{hop}} [E_0 - H_0]^{-1} h^{\text{hop}} | 2, 0 \rangle \\ &= \frac{1}{2} \langle 2, 0 | h^{\text{hop}} [E_0 - H_0]^{-1} h^{\text{hop}} | 0, 2 \rangle \end{aligned} \quad (\text{D17})$$

The factor  $1/2$  is put to take into account just the single-site energy out of the corresponding two-site energy. As for the hopping along the  $x$ -axis, we have:

$$\begin{aligned} &\frac{1}{2} \langle 0, 2 | h^{x\text{-hop}} [E_0 - H_0]^{-1} h^{x\text{-hop}} | 0, 2 \rangle \\ &= \frac{1}{2} \langle 0, 2 | h^{x\text{-hop}} [E_0 - H_0]^{-1} \left( -\frac{i}{2} \right) | 1, 1 \rangle \\ &= \left( \frac{-i}{4} \right) \langle 0, 2 | h^{x\text{-hop}} \left[ -\frac{3g^2}{16} (\Gamma_j + \Gamma_{j+\mu_x}) \right]^{-1} | 1, 1 \rangle \\ &= \left( \frac{-i}{4} \right) \langle 0, 2 | h^{x\text{-hop}} \left( -\frac{8}{3g^2} \right) | 1, 1 \rangle \\ &= \frac{2i}{3g^2} \langle 0, 2 | \left( \frac{i}{2} \right) | 0, 2 \rangle = \boxed{-\frac{1}{3g^2}} \end{aligned} \quad (\text{D18})$$

Analogously proceeding, we have:

$$\frac{1}{2} \langle 2, 0 | h^{x\text{-hop}} [E_0 - H_0]^{-1} h^{x\text{-hop}} | 0, 2 \rangle = \boxed{\frac{1}{3g^2}} \quad (\text{D19})$$

Then, the  $2^{nd}$ -order perturbative  $x$ -hopping term reads:

$$\begin{aligned} h_{x\text{-hop}}^{\text{eff}} &= -\frac{1}{3g^2} \begin{pmatrix} 0 & 0 & 0 & 0 \\ 0 & +1 & -1 & 0 \\ 0 & -1 & +1 & 0 \\ 0 & 0 & 0 & 0 \end{pmatrix} \\ &= -\frac{1}{6g^2} \left[ \sigma_j^x \sigma_{j+\mu_y}^x + \sigma_j^y \sigma_{j+\mu_y}^y - \sigma_j^z \sigma_{j+\mu_y}^z \right] \end{aligned} \quad (\text{D20})$$

As for the  $y$ -hopping Hamiltonian, one can prove that:

$$\begin{aligned} H_{y\text{-hop}}^{\text{eff}} &= \frac{1}{3g^2} \begin{pmatrix} 0 & 0 & 0 & 0 \\ 0 & +1 & +1 & 0 \\ 0 & +1 & +1 & 0 \\ 0 & 0 & 0 & 0 \end{pmatrix} \\ &= -\frac{1}{6g^2} \left[ \sigma_j^x \sigma_{j+\mu_y}^x + \sigma_j^y \sigma_{j+\mu_y}^y + \sigma_j^z \sigma_{j+\mu_y}^z \right] \end{aligned} \quad (\text{D21})$$

Summarizing, in the large- $g$  limit, the Hamiltonian in

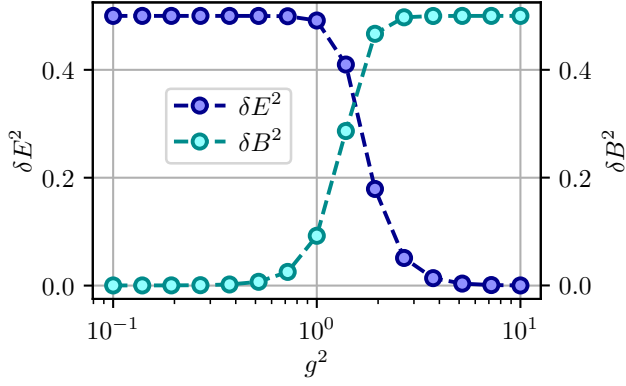


Figure 13. Quantum fluctuations of the gauge observables in Eq. (8)-(9) as a function of the  $g$ -coupling. Results obtained from simulations of a  $2 \times 2$  lattice in OBC.

Eq. (B31) can be approximated as:

$$H^{\text{eff}} \sim -\frac{1}{6g^2} \sum_{\mathbf{j}, \mu_x} \left[ \sigma_{\mathbf{j}}^x \sigma_{\mathbf{j}+\mu_x}^x + \sigma_{\mathbf{j}}^y \sigma_{\mathbf{j}+\mu_x}^y - \sigma_{\mathbf{j}}^z \sigma_{\mathbf{j}+\mu_x}^z \right] - \frac{1}{6g^2} \sum_{\mathbf{j}, \mu_y} \left[ \sigma_{\mathbf{j}}^x \sigma_{\mathbf{j}+\mu_y}^x + \sigma_{\mathbf{j}}^y \sigma_{\mathbf{j}+\mu_y}^y + \sigma_{\mathbf{j}}^z \sigma_{\mathbf{j}+\mu_y}^z \right] \quad (\text{D22})$$

which looks similar to a 2D quantum Heisenberg Hamiltonian apart from the staggering factor in the kinetic term  $\sigma^z \sigma^z$ .

## Appendix E: Exact Diagonalization results

As pointed out in Sec. II, addressing the 2D SU(2) LGT on large system sizes is significantly demanding, especially in the small- $g$  (magnetic) phase and close to the  $g$ -transition, because of the large entanglement displayed by the model. Nevertheless, by exploiting ED simulations, we can provide compelling features of both the pure and the full SU(2) theories.

As for the pure theory, we show in Fig. 13 that the magnetic and the electric phases discussed in Sec. II A are characterized by strong fluctuations

$$\delta E^2 = \sqrt{\langle E^4 \rangle - \langle E^2 \rangle^2} \quad \delta B^2 = \sqrt{\langle B^4 \rangle - \langle B^2 \rangle^2} \quad (\text{E1})$$

of the gauge observables in Eq. (8)-(9) respectively. In particular, the magnetic (small- $g$ ) phase is characterized by large and strong fluctuating electric energy, while the electric (large- $g$ ) phase displays large and strong fluctuating magnetic energy.

As for the full SU(2) theory, to select the chosen baryon density sector  $b^*$  in ED simulations, we add to Eq. (B31)

the term

$$H_b = \tilde{\eta} \left( \sum_{\mathbf{j} \in \Lambda} \sum_{\alpha} \psi_{\mathbf{j}, \alpha}^{\dagger} \psi_{\mathbf{j}, \alpha} + 2 - 2b^* \right)^2 \quad (\text{E2})$$

where  $\tilde{\eta}$  plays the role of a large penalty coefficient that increases the energy associated with baryon number densities differing from  $b^*$ . When exploiting TTN methods, the chosen symmetry sector is externally selected by directly encoding the abelian symmetry  $U(1)$  in the TTN ansatz [22, 24, 102, 103].

In Fig. 14, we focus on the local observables in Eq. (8)-(9)-(11) and the entanglement entropy in Eq. (14) resulting from ED simulations in OBC at  $b = 0$  and  $b = 0.5$ . By varying  $m \in [10^{-1}, 10^0]$ , we notice that, for both the baryon-density sectors, the larger the mass  $m$ , the sharper the transition between the *magnetic* (small- $g$ ) and the *electric* (large- $g$ ) phases.

Moreover, as discussed in Sec. II C, in between the two phases, the model is characterized by a *baryon-liquid phase*, where the particle density  $\varrho$  defined in Eq. (11) reveals peaked and strong fluctuating (check also Fig. 15(a)-(b)), and the peak is higher and larger for smaller  $m$ -values.

Correspondingly, for fixed  $m$ -values, the entanglement entropy of half the lattice is constant in the magnetic phase, peaked in the  $g$ -transition, and tending to a default value (0 for  $b = 0$  and 1 for  $b = 0.5$ ) in the electric phase. In the limit of large masses, this peak in the entropy progressively vanishes, and we recover the (*crossover/first-order*) transition observed in Fig. 2 for the pure theory.

Within the Baryon-liquid phase, we can also notice a non-null value of the color density defined in Eq. (13), which is related to the presence of single particle non-null expectation values. As shown in Fig. 15,  $|\hat{\mathbf{S}}|^2$  displays a peak in the proximity of the magnetic-electric  $g$ -transition and is supported by fluctuations  $\delta|\hat{\mathbf{S}}|^2$  of the same order of magnitude of the observable itself. In these terms, this phase represents the only candidate for displaying deconfinement. At any rate, it does not survive in the continuum limit, as it remains bound in intermediate  $g$ -values.

## Appendix F: Tensor Network Methods

Tensor network simulations performed in this work have used the Tree Tensor Networks ground state variational searching algorithm [24, 53, 54]. Given the Hamiltonian of the considered system, the unconstrained binary TTN is constructed, and the ground state is determined by optimizing all the tensors in the tree network with a fixed bond dimension  $\chi$ .

In detail, we exploit the Krylov sub-space expansion technique to numerically solve the local eigenvalue problem for each tensor [24]. This step is carried out efficiently by applying the Arnoldi method of the ARPACK library

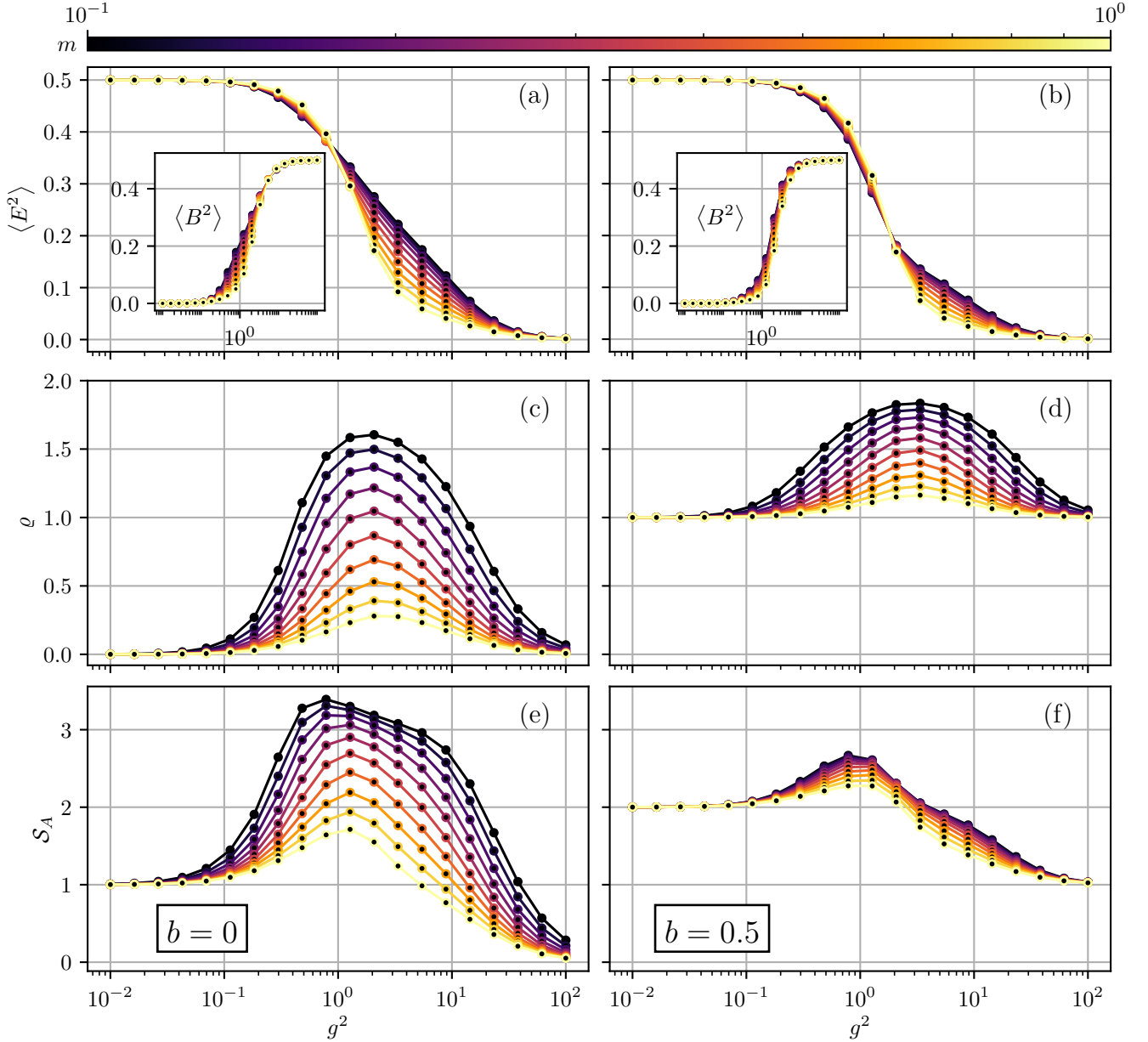


Figure 14. Simulations of the full SU(2) Hamiltonian in Eq. (B31) on a  $2 \times 2$  lattice with OBC in the  $b = 0$  (a)-(c)-(e) and  $b = 0.5$  (b)-(d)-(f) baryon number density sectors. The plots display respectively: (a)-(b) the average electric and magnetic energy contributions  $\langle E^2 \rangle$  and  $\langle B^2 \rangle$  (inset) enlightening the transition between the magnetic and the electric phases discussed in Sec. II A; (c)-(d) the average particle density  $\rho$  in Eq. (11), which appears peaked in the  $g$ -transition; (e)-(f) the entanglement entropy  $S_A$  of half the system, with a peak in the  $g$ -transition which is larger for smaller  $m$  while disappearing for large ones.

[104]. The optimization is sequentially iterated for all the tensors in the tree network. The whole procedure (sweep) is repeated as long as the total energy does not converge to a minimal value. As for the single-node optimization of the Tensor Network, we set the Arnoldi algorithm to discard singular values smaller than  $10^{-4}$ . Then, the convergence of the whole TN algorithm relies on absolute and relative convergence thresholds  $\Delta\varepsilon_{abs} = 10^{-5}$

and  $\Delta\varepsilon_{rel} = 10^{-5}$  defined respectively as

$$\Delta\varepsilon_{abs} \equiv |\varepsilon_{n-1} - \varepsilon_n| \quad \Delta\varepsilon_{rel} \equiv \left| \frac{\varepsilon_{n-1} - \varepsilon_n}{\varepsilon_n} \right| \quad (\text{F1})$$

for energy values  $\varepsilon_{n-1}$  and  $\varepsilon_n$  arisen from consecutive optimization sweeps  $n-1$  and  $n$ . Ultimately, the maximal bond dimension  $\chi$  adopted in the reported TN simulations is always obtained by looking at the single-site



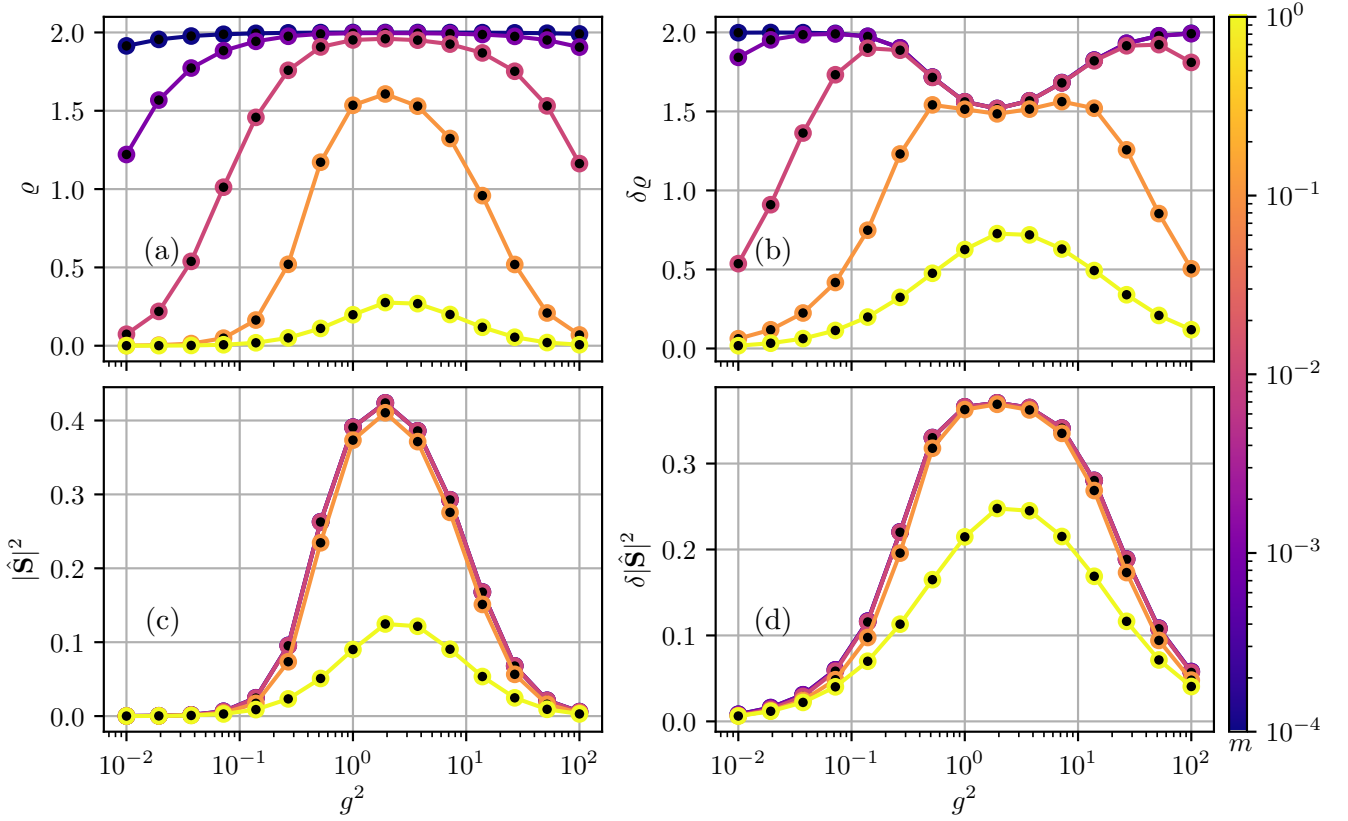


Figure 15. ED simulations of a  $2 \times 2$  lattice in PBC. The plots display respectively: (a) the average particle density  $\rho$  and (b) its quantum fluctuations  $\delta\rho$ ; (c) the matter color density  $|\mathbf{S}|^2$  and (d) its quantum fluctuations  $\delta|\mathbf{S}|^2$ . All the observables are studied as a function of the square coupling  $g^2$  for different mass values  $m \in [10^{-4}, 10^1]$ .

energy relative convergence of  $10^{-4}$  (see Fig. 16).

- 
- [1] J. B. Kogut, *Reviews of Modern Physics* **51**, 659 (1979).
  - [2] H. J. Rothe, *Lattice Gauge Theories: An Introduction (Fourth Edition)* (World Scientific Publishing Company, 2012).
  - [3] K. G. Wilson, *Physical Review D* **10**, 2445 (1974).
  - [4] J. B. Kogut, *Reviews of Modern Physics* **55**, 775 (1983).
  - [5] R. Gupta, Introduction to Lattice QCD (1998), [arxiv:hep-lat/9807028](https://arxiv.org/abs/hep-lat/9807028).
  - [6] J. Kogut, M. Stone, H. W. Wyld, J. Shigemitsu, S. H. Shenker, and D. K. Sinclair, *Physical Review Letters* **48**, 1140 (1982).
  - [7] S. Gottlieb, W. Liu, D. Toussaint, R. L. Renken, and R. L. Sugar, *Physical Review D* **35**, 3972 (1987).
  - [8] M. Alford, K. Rajagopal, and F. Wilczek, *Nuclear Physics B* **537**, 443 (1999).
  - [9] M. Mitter, J. M. Pawłowski, and N. Strodthoff, *Physical Review D* **91**, 054035 (2015).
  - [10] M. Creutz, *Physical Review D* **21**, 2308 (1980).
  - [11] M. Creutz and K. J. M. Moriarty, *Physical Review D* **26**, 2166 (1982).
  - [12] J. Kogut, J. Polonyi, H. W. Wyld, J. Shigemitsu, and D. K. Sinclair, *Nuclear Physics B* **251**, 311 (1985).
  - [13] M. Biswal, M. Deka, S. Digal, and P. S. Saumia, *Physical Review D* **96**, 014503 (2017).
  - [14] E. Y. Loh, J. E. Gubernatis, R. T. Scalettar, S. R. White, D. J. Scalapino, and R. L. Sugar, *Physical Review B* **41**, 9301 (1990).
  - [15] M. Troyer and U.-J. Wiese, *Physical Review Letters* **94**, 170201 (2005).
  - [16] E. A. Martinez, C. A. Muschik, P. Schindler, D. Nigg, A. Erhard, M. Heyl, P. Hauke, M. Dalmonte, T. Monz, P. Zoller, and R. Blatt, *Nature* **534**, 516 (2016).
  - [17] C. Schweizer, F. Grusdt, M. Berngruber, L. Barbiero, E. Demler, N. Goldman, I. Bloch, and M. Aidelsburger, *Nature Physics* **15**, 1168 (2019).
  - [18] B. Yang, H. Sun, R. Ott, H.-Y. Wang, T. V. Zache, J. C. Halimeh, Z.-S. Yuan, P. Hauke, and J.-W. Pan, *Nature* **587**, 392 (2020).
  - [19] Z.-Y. Zhou, G.-X. Su, J. C. Halimeh, R. Ott, H. Sun, P. Hauke, B. Yang, Z.-S. Yuan, J. Berges, and J.-W. Pan, *Science* **377**, 311 (2022).
  - [20] N. H. Nguyen, M. C. Tran, Y. Zhu, A. M. Green, C. H. Alderete, Z. Davoudi, and N. M. Linke, *PRX Quantum* **3**, 020324 (2022).

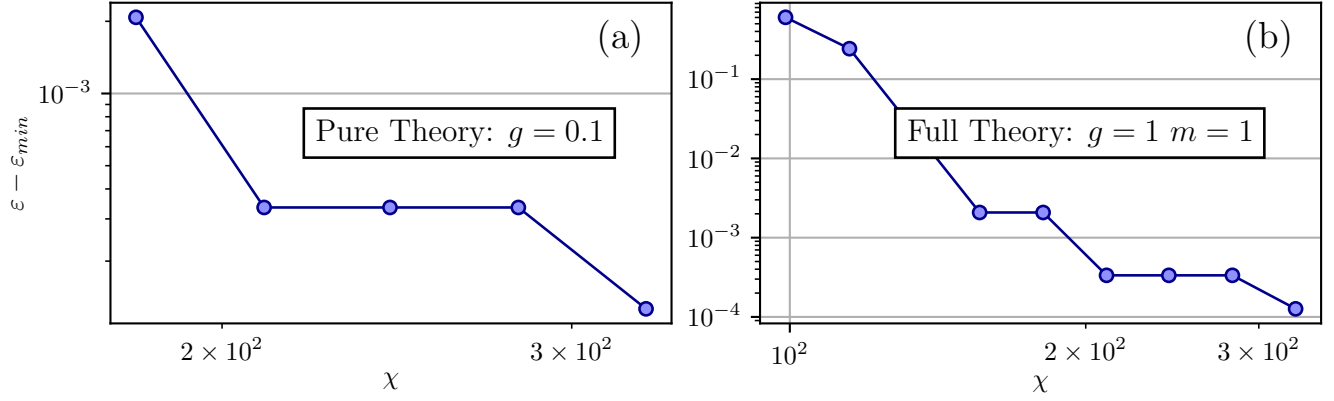


Figure 16. Convergence tests for (a) the pure Eq. (B32) and the (b) full Eq. (B31) Hamiltonian on a  $4 \times 4$  lattice in OBC. The plots display the scaling of the ground-state energy density  $\varepsilon$  (up to its minimal value  $\varepsilon_{min}$ ) as a function of the bond dimension  $\chi$  adopted in the TTN simulations. In the plots

- [21] F. Verstraete, V. Murg, and J. Cirac, *Advances in Physics* **57**, 143 (2008).
- [22] R. Orús, *Nature Reviews Physics* **1**, 538 (2019).
- [23] S. Montangero, *Introduction to Tensor Network Methods* (Springer International Publishing, 2018).
- [24] P. Silvi, F. Tschirsich, M. Gerster, J. Jünemann, D. Jaschke, M. Rizzi, and S. Montangero, *SciPost Physics Lecture Notes*, 008 (2019).
- [25] M. Bañuls, K. Cichy, J. Cirac, and K. Jansen, *Journal of High Energy Physics* **2013**, 158 (2013).
- [26] E. Rico, T. Pichler, M. Dalmonte, P. Zoller, and S. Montangero, *Physical Review Letters* **112**, 201601 (2014).
- [27] S. Kühn, J. I. Cirac, and M.-C. Bañuls, *Physical Review A* **90**, 042305 (2014).
- [28] M. C. Bañuls, K. Cichy, J. I. Cirac, K. Jansen, and H. Saito, *Physical Review D* **92**, 034519 (2015).
- [29] B. Buyens, F. Verstraete, and K. Van Acoleyen, *Physical Review D* **94**, 085018 (2016).
- [30] B. Buyens, S. Montangero, J. Haegeman, F. Verstraete, and K. Van Acoleyen, *Physical Review D* **95**, 094509 (2017).
- [31] B. Buyens, J. Haegeman, F. Hebenstreit, F. Verstraete, and K. Van Acoleyen, *Physical Review D* **96**, 114501 (2017).
- [32] E. Ercolessi, P. Facchi, G. Magnifico, S. Pascazio, and F. V. Pepe, *Physical Review D* **98**, 074503 (2018).
- [33] G. Magnifico, D. Vodola, E. Ercolessi, S. P. Kumar, M. Müller, and A. Bermudez, *Physical Review D* **99**, 014503 (2019).
- [34] G. Magnifico, D. Vodola, E. Ercolessi, S. P. Kumar, M. Müller, and A. Bermudez, *Physical Review B* **100**, 115152 (2019).
- [35] L. Funcke, K. Jansen, and S. Kühn, *Physical Review D* **101**, 054507 (2020).
- [36] G. Magnifico, M. Dalmonte, P. Facchi, S. Pascazio, F. V. Pepe, and E. Ercolessi, *Quantum* **4**, 281 (2020).
- [37] M. Rigobello, S. Notarnicola, G. Magnifico, and S. Montangero, *Physical Review D* **104**, 114501 (2021).
- [38] M. C. Bañuls, M. P. Heller, K. Jansen, J. Knaute, and V. Svensson, "A quantum information perspective on meson melting," (2022), [arxiv:2206.10528](#) [cond-mat, physics:hep-ph, physics:hep-th, physics:quant-ph].
- [39] L. Funcke, T. Hartung, K. Jansen, and S. Kühn, "Review on Quantum Computing for Lattice Field Theory," (2023), [arxiv:2302.00467](#) [hep-lat, physics:quant-ph].
- [40] T. Felser, P. Silvi, M. Collura, and S. Montangero, *Physical Review X* **10**, 041040 (2020).
- [41] G. Magnifico, T. Felser, P. Silvi, and S. Montangero, *Nature Communications* **12**, 3600 (2021).
- [42] P. Emonts, A. Kelman, U. Borla, S. Moroz, S. Gazit, and E. Zohar, "Finding the ground state of a lattice gauge theory with fermionic tensor networks: A  $\mathbb{Z}_2$  demonstration," (2022), [arxiv:2211.00023](#) [cond-mat, physics:hep-lat, physics:quant-ph].
- [43] P. Silvi, E. Rico, M. Dalmonte, F. Tschirsich, and S. Montangero, *Quantum* **1**, 9 (2017).
- [44] P. Silvi, Y. Sauer, F. Tschirsich, and S. Montangero, *Physical Review D* **100**, 074512 (2019).
- [45] S. V. Kadam, I. Raychowdhury, and J. Stryker, in *Proceedings of The 39th International Symposium on Lattice Field Theory — PoS(LATTICE2022)*, Vol. 430 (SISSA Medialab, 2023) p. 373.
- [46] D. Horn, *Physics Letters B* **100**, 149 (1981).
- [47] P. Orland and D. Rohrlich, *Nuclear Physics B* **338**, 647 (1990).
- [48] S. Chandrasekharan and U. J. Wiese, *Nuclear Physics B* **492**, 455 (1997).
- [49] R. Brower, S. Chandrasekharan, and U.-J. Wiese, *Physical Review D* **60**, 094502 (1999).
- [50] L. Tagliacozzo, A. Celi, and M. Lewenstein, *Physical Review X* **4**, 041024 (2014).
- [51] J. Eisert, M. Cramer, and M. B. Plenio, *Reviews of Modern Physics* **82**, 277 (2010).
- [52] Y. Meurice, J. C. Osborn, R. Sakai, J. Unmuth-Yockey, S. Catterall, and R. D. Somma, "Tensor networks for High Energy Physics: Contribution to Snowmass 2021," (2022), [arxiv:2203.04902](#) [hep-lat, physics:hep-th].
- [53] G. Cataldi, A. Abedi, G. Magnifico, S. Notarnicola, N. D. Pozza, V. Giovannetti, and S. Montangero, *Quantum* **5**, 556 (2021).
- [54] G. Ferrari, G. Magnifico, and S. Montangero, *Physical Review B* **105**, 214201 (2022).

- [55] E. Zohar, *Physical Review Research* **3**, 033179 (2021).
- [56] J. F. Haase, L. Dellantonio, A. Celi, D. Paulson, A. Kan, K. Jansen, and C. A. Muschik, *Quantum* **5**, 393 (2021).
- [57] E. Zohar, J. I. Cirac, and B. Reznik, *Physical Review Letters* **110**, 125304 (2013).
- [58] T. Byrnes and Y. Yamamoto, *Physical Review A* **73**, 022328 (2006).
- [59] S. V. Mathis, G. Mazzola, and I. Tavernelli, *Physical Review D* **102**, 094501 (2020).
- [60] Z. Davoudi, M. Hafezi, C. Monroe, G. Pagano, A. Seif, and A. Shaw, *Physical Review Research* **2**, 023015 (2020).
- [61] G. Mazzola, S. V. Mathis, G. Mazzola, and I. Tavernelli, *Physical Review Research* **3**, 043209 (2021).
- [62] A. Kan, L. Funcke, S. Kühn, L. Dellantonio, J. Zhang, J. F. Haase, C. A. Muschik, and K. Jansen, *Physical Review D* **104**, 034504 (2021).
- [63] E. Zohar, *Philosophical Transactions of the Royal Society A: Mathematical, Physical and Engineering Sciences* **380**, 20210069 (2021).
- [64] A. Mariani, S. Pradhan, and E. Ercolessi, “Hamiltonians and gauge-invariant Hilbert space for lattice Yang-Mills-like theories with finite gauge group,” (2023), [arxiv:2301.12224 \[hep-lat, physics:quant-ph\]](#).
- [65] D. Pomarico, L. Cosmai, P. Facchi, C. Lupo, S. Pascazio, and F. V. Pepe, *Entropy* **25**, 608 (2023).
- [66] C. W. Bauer, Z. Davoudi, N. Klco, and M. J. Savage, *Nature Reviews Physics* **5**, 420 (2023).
- [67] D. Banerjee, M. Bögli, M. Dalmonte, E. Rico, P. Stebler, U.-J. Wiese, and P. Zoller, *Physical Review Letters* **110**, 125303 (2013).
- [68] U.-J. Wiese, *Annalen der Physik* **525**, 777 (2013), [arxiv:1305.1602](#).
- [69] L. Tagliacozzo, A. Celi, P. Orland, M. W. Mitchell, and M. Lewenstein, *Nature Communications* **4**, 2615 (2013), [arxiv:1211.2704](#).
- [70] A. Mezzacapo, E. Rico, C. Sabín, I. L. Egusquiza, L. Lamata, and E. Solano, *Physical Review Letters* **115**, 240502 (2015).
- [71] M. C. Bañuls and K. Cichy, *Reports on Progress in Physics* **83**, 024401 (2020).
- [72] M. C. Bañuls, R. Blatt, J. Catani, A. Celi, J. I. Cirac, M. Dalmonte, L. Fallani, K. Jansen, M. Lewenstein, S. Montangero, C. A. Muschik, B. Reznik, E. Rico, L. Tagliacozzo, K. Van Acoleyen, F. Verstraete, U.-J. Wiese, M. Wingate, J. Zakrzewski, and P. Zoller, *The European Physical Journal D* **74**, 165 (2020).
- [73] Y. Y. Atas, J. Zhang, R. Lewis, A. Jahanpour, J. F. Haase, and C. A. Muschik, *Nature Communications* **12**, 6499 (2021).
- [74] N. Klco, A. Roggero, and M. J. Savage, *Reports on Progress in Physics* **85**, 064301 (2022).
- [75] S. Catterall, R. Harnik, V. E. Hubeny, C. W. Bauer, A. Berlin, Z. Davoudi, T. Faulkner, T. Hartman, M. Headrick, Y. F. Kahn, H. Lamm, Y. Meurice, S. Rajendran, M. Rangamani, and B. Swingle, “Report of the Snowmass 2021 Theory Frontier Topical Group on Quantum Information Science,” (2022).
- [76] Y. Y. Atas, J. F. Haase, J. Zhang, V. Wei, S. M.-L. Pfaendler, R. Lewis, and C. A. Muschik, “Simulating one-dimensional quantum chromodynamics on a quantum computer: Real-time evolutions of tetra- and pentaquarks,” (2023), [arxiv:2207.03473 \[hep-lat, physics:hep-ph, physics:quant-ph\]](#).
- [77] Z. Davoudi, A. F. Shaw, and J. R. Stryker, “General quantum algorithms for Hamiltonian simulation with applications to a non-Abelian lattice gauge theory,” (2023), [arxiv:2212.14030 \[hep-lat, physics:hep-ph, physics:nucl-th, physics:quant-ph\]](#).
- [78] Y. Zhou, E. M. Stoudenmire, and X. Waintal, *Physical Review X* **10**, 041038 (2020).
- [79] T. Ayril, T. Louvet, Y. Zhou, C. Lambert, E. M. Stoudenmire, and X. Waintal, *PRX Quantum* **4**, 020304 (2023).
- [80] P. Silvi, E. Rico, T. Calarco, and S. Montangero, *New Journal of Physics* **16**, 103015 (2014).
- [81] E. Zohar and J. I. Cirac, *Physical Review D* **97**, 034510 (2018).
- [82] E. Zohar and J. I. Cirac, *Physical Review D* **99**, 114511 (2019).
- [83] J. Kogut and L. Susskind, *Physical Review D* **11**, 395 (1975).
- [84] L. Susskind, *Physical Review D* **16**, 3031 (1977).
- [85] T. V. Zache, F. Hebenstreit, F. Jendrzewski, M. K. Oberthaler, J. Berges, and P. Hauke, *Quantum Science and Technology* **3**, 034010 (2018).
- [86] E. Zohar and J. I. Cirac, *Physical Review B* **98**, 075119 (2018).
- [87] Y. R. Wang, *Physical Review B* **43**, 3786 (1991).
- [88] U. J. Wiese and H. P. Ying, *Zeitschrift für Physik B Condensed Matter* **93**, 147 (1994).
- [89] J. Giedt, *International Journal of Modern Physics A* **31**, 1630011 (2016).
- [90] A. Kitaev, *Annals of Physics January Special Issue*, **321**, 2 (2006).
- [91] B. Svetitsky and L. G. Yaffe, *Nuclear Physics B* **210**, 423 (1982).
- [92] L. Tagliacozzo and G. Vidal, *Physical Review B* **83**, 115127 (2011).
- [93] M. Engelhardt, K. Langfeld, H. Reinhardt, and O. Teneert, *Physical Review D* **61**, 054504 (2000).
- [94] T. Felser, S. Notarnicola, and S. Montangero, *Physical Review Letters* **126**, 170603 (2021).
- [95] A. Di Meglio, K. Jansen, I. Tavernelli, C. Alexandrou, S. Arunachalam, C. W. Bauer, K. Borras, S. Carranza, A. Crippa, V. Croft, R. de Putter, A. Delgado, V. Dunjko, D. J. Egger, E. Fernandez-Combarro, E. Fuchs, L. Funcke, D. Gonzalez-Cuadra, M. Grossi, J. C. Halimeh, Z. Holmes, S. Kuhn, D. Lacroix, R. Lewis, D. Lucchesi, M. L. Martinez, F. Meloni, A. Mezzacapo, S. Montangero, L. Nagano, V. Radescu, E. R. Ortega, A. Roggero, J. Schuhmacher, J. Seixas, P. Silvi, P. Spentzouris, F. Tacchino, K. Temme, K. Terashi, J. Tura, C. Tuysuz, S. Vallecorsa, U.-J. Wiese, S. Yoo, and J. Zhang, “Quantum Computing for High-Energy Physics: State of the Art and Challenges. Summary of the QC4HEP Working Group,” (2023), [arxiv:2307.03236 \[hep-ex, physics:hep-lat, physics:hep-th, physics:quant-ph\]](#).
- [96] M. Rigobello, “*Rgbmrc/simsio*,” Zenodo (2023).
- [97] E. Zohar and M. Burrello, *Physical Review D* **91**, 054506 (2015).
- [98] P. Jordan and E. Wigner, *Zeitschrift für Physik* **47**, 631 (1928).
- [99] F. Verstraete and J. I. Cirac, *Journal of Statistical Mechanics: Theory and Experiment* **2005**, P09012 (2005).
- [100] P. Corboz, R. Orús, B. Bauer, and G. Vidal, *Physical Review B* **81**, 165104 (2010).

- [101] C. V. Kraus, N. Schuch, F. Verstraete, and J. I. Cirac, [Physical Review A \*\*81\*\*, 052338 \(2010\)](#).
- [102] S. Singh, R. N. C. Pfeifer, and G. Vidal, [Physical Review A \*\*82\*\*, 050301 \(2010\)](#).
- [103] S. Singh, R. N. C. Pfeifer, and G. Vidal, [Physical Review B \*\*83\*\*, 115125 \(2011\)](#).
- [104] R. B. Lehoucq, D. C. Sorensen, and C. Yang, *ARPACK Users' Guide: Solution of Large-scale Eigenvalue Problems with Implicitly Restarted Arnoldi Methods* (SIAM, 1998).